INTERNATIONAL JOURNAL FOR NUMERICAL METHODS IN FLUIDS
Int. J. Numer. Meth. Fluids 2001; **37**: 541–575 (DOI: 10.1002/fld.186)

A Petrov–Galerkin finite element model for one-dimensional fully non-linear and weakly dispersive wave propagation

Seung-Buhm Woo and Philip L.-F. Liu*

School of Civil and Environmental Engineering, Cornell University, Ithaca, NY, U.S.A.

SUMMARY

A new finite element method is presented to solve one-dimensional depth-integrated equations for fully non-linear and weakly dispersive waves. For spatial integration, the Petrov–Galerkin weighted residual method is used. The weak forms of the governing equations are arranged in such a way that the shape functions can be piecewise linear, while the weighting functions are piecewise cubic with C^2-continuity. For the time integration an implicit predictor–corrector iterative scheme is employed. Within the framework of linear theory, the accuracy of the scheme is discussed by considering the truncation error at a node. The leading truncation error is fourth-order in terms of element size. Numerical stability of the scheme is also investigated. If the Courant number is less than 0.5, the scheme is unconditionally stable. By increasing the number of iterations and/or decreasing the element size, the stability characteristics are improved significantly. Both Dirichlet boundary condition (for incident waves) and Neumann boundary condition (for a reflecting wall) are implemented. Several examples are presented to demonstrate the range of applicabilities and the accuracy of the model. Copyright © 2001 John Wiley & Sons, Ltd.

KEY WORDS: extended Boussinesq equations; fully non-linear; Petrov–Galerkin FEM

1. INTRODUCTION

For many near-shore hydrodynamic processes, such as wave shoaling, wave breaking and wave agitations in a harbor, non-linearity and frequency dispersion are equally important. In recent years, several mathematical models have been proposed to describe fully non-linear and weakly dispersive wave propagation [1–4]. High-order finite difference schemes have been implemented to find solutions of these mathematical models [5–7]. However, difficulties in modeling irregular geometries in two space dimensions with structured finite difference grids can lead to a loss of accuracy in these schemes.

* Correspondence to: School of Civil and Environmental Engineering, Hollister Hall, Cornell University, Ithaca, NY 14853-3501, U.S.A.

Received May 2000
Revised October 2000

The alternative is to use unstructured finite element methods (FEM) to model the wave propagation in a geometrically complex domain. Due to the flexibility of an unstructured grid system, an additional benefit for using FEM is that the number of nodal points can be minimized by using a fine resolution only in the region of interest or in the region with rapidly changing depth. Several FEM models have been developed for the conventional Boussinesq equations, in which non-linearity and frequency dispersion are equally weak [8–12]. The primary differences among these models are the time integration scheme and the type of finite elements used. However, since the highest order of spatial derivatives in the Boussinesq equations is only second order, all the existing FEM models used either linear triangular elements or linear rectangular elements.

It is only recently that research papers have been published on FEMs for extended Boussinesq equations in which additional frequency dispersion terms are added to the conventional Boussinesq equations so that the resulting model equations are applicable in relatively deep water. Since the highest spatial derivative term in the extended Boussinesq equations is third order, the linear Galerkin FEM can no longer be applied directly. A common approach to reduce the order of differentiation is to introduce auxiliary variables, which are first or second spatial derivatives of the free surface displacement and/or the velocity components, depending on the formulation. While linear elements can be used, additional unknowns and equations must be solved in the resulting coupled systems [13–15].

It appears that no attempt has been made to develop an FEM for the fully non-linear and weakly dispersive wave equations. In the governing equations for fully non-linear waves, the third spatial derivatives appear in both momentum and continuity equations. In this paper, we develop a Petrov–Galerkin weighted residual method to solve the one-dimensional problem. The weak forms of the governing equations are arranged in such a way that piecewise linear shape functions and piecewise cubic spline weighting functions can be applied. The proposed spatial discretization methods are similar to those introduced by Sanz-Serna and Christie [16] for the KdV equation. Moreover, in the present FEM formulation, the product approximation is used for the treatment of non-linear terms. The product approximation has been successfully applied to a number of non-linear problems [17], including the KdV equation [16] and the non-linear Schrödinger equation [18].

This paper is organized in the following manner. In the following section, the governing equations for fully non-linear and weakly dispersive waves are summarized. In Section 3, the proposed numerical scheme is discussed in detail. The accuracy and the stability characteristics of the proposed numerical scheme are also discussed. Numerical examples are given in Section 4, which demonstrate the range of applicability and the accuracy of the proposed numerical scheme. In Appendix A, the detailed information for the mass matrix, forcing vector and boundary vector for the matrix equation are given.

2. ONE-DIMENSIONAL GOVERNING EQUATIONS FOR FULLY NON-LINEAR AND WEAKLY DISPERSIVE WAVES

The physical system can be characterized by a typical wave amplitude, a, a typical water depth, h_0, and a typical wave number, k_0. Two dimensionless parameters

$$\varepsilon = \frac{a}{h_0} \tag{2.1}$$

and

$$\mu^2 = (k_0 h_0)^2 \tag{2.2}$$

represent the non-linearity and frequency dispersion in the system espectively. The Boussinesq wave theory requires $O(\varepsilon) \approx O(\mu^2) \ll O(1)$ so that the theory can be only applied in fairly shallow water and for weakly non-linear waves. For the fully non-linear and weakly dispersive wave theory, the non-linear effects are completely retained, i.e., $O(\varepsilon) = O(1)$, while the frequency dispersion is still assumed to be weak, i.e., $O(\mu^2) \ll O(1)$. The governing equations for fully non-linear and weakly dispersive waves have been derived by several researchers [1–4]. In this paper, only the one-dimensional problems are investigated.

Following Liu's [1] notation, the one-dimensional continuity and momentum equations can be expressed as

$$\frac{\partial \eta}{\partial t} + \frac{\partial M}{\partial x} = O(\mu^4) \tag{2.3}$$

$$\frac{\partial u_\alpha}{\partial t} + \varepsilon u_\alpha \frac{\partial u_\alpha}{\partial x} + \frac{\partial \eta}{\partial x} + \mu^2 V_1 + \varepsilon \mu^2 V_2 = O(\mu^4) \tag{2.4}$$

in which

$$M = M_1 + M_2 \tag{2.5a}$$

$$M_1 = (h + \varepsilon\eta) u_\alpha \tag{2.5b}$$

$$M_2 = \mu^2 (h + \varepsilon\eta) \left\{ \left[\frac{1}{2} z_\alpha^2 - \frac{1}{6} (h^2 - \varepsilon\eta h + (\varepsilon\eta)^2) \right] \frac{\partial^2 u_\alpha}{\partial x^2} + \left[z_\alpha + \frac{1}{2} (h - \varepsilon\eta) \right] \frac{\partial^2 h u_\alpha}{\partial x^2} \right\} \tag{2.5c}$$

$$V_1 = \frac{1}{2} z_\alpha^2 \frac{\partial^3 u_\alpha}{\partial t\, \partial x^2} + z_\alpha \frac{\partial^2}{\partial x^2} \left(h \frac{\partial u_\alpha}{\partial t} \right) - \frac{\partial}{\partial x} \left[\frac{1}{2} (\varepsilon\eta)^2 \frac{\partial^2 u_\alpha}{\partial t\, \partial x} + \varepsilon\eta \frac{\partial}{\partial x} \left(h \frac{\partial u_\alpha}{\partial t} \right) \right] \tag{2.5d}$$

$$V_2 = \frac{\partial}{\partial x} \left[(z_\alpha - \varepsilon\eta) u_\alpha \frac{\partial^2 h u_\alpha}{\partial x^2} + \frac{1}{2} (z_\alpha^2 - (\varepsilon\eta)^2) u_\alpha \frac{\partial^2 u_\alpha}{\partial x^2} + \frac{1}{2} \left(\frac{\partial h u_\alpha}{\partial x} + \varepsilon\eta \frac{\partial u_\alpha}{\partial x} \right)^2 \right] \tag{2.5e}$$

where η is the free surface displacement, u_α the horizontal velocity evaluated at $z = z_\alpha$, h the water depth, and z the co-ordinate measured upwards from the still-water level. We remark here that although the order of accuracy of the above equations is of $O(\mu^4)$, the linear dispersion characteristics of these equations can be improved further by choosing z_α properly. For instance, Chen and Liu [19] suggested that in order to apply these equations in the intermediate to deep-water, the optimal value for z_α should be $-0.52h$. Detailed discussions of

this choice are given in Chen and Liu [19] and Nwogu [20]. It is reiterated here that the third spatial derivatives of the velocity appear in both governing equations.

3. NUMERICAL SCHEMES

In this section, the spatial and time integration schemes used to find solutions for (2.3) and (2.4) are discussed.

3.1. Petrov–Galerkin FEM

Within the computational domain, $0 < x < L$, a weighted residual method is used. Thus, requiring the weighted residuals of the governing equations (2.3) and (2.4) to be zero results in

$$\int_0^L w\left\{\frac{\partial \eta}{\partial t}+\frac{\partial M}{\partial x}\right\}\mathrm{d}x=0 \tag{3.1}$$

and

$$\int_0^L w\left\{\frac{\partial u_\alpha}{\partial t}+\varepsilon u_\alpha\frac{\partial u_\alpha}{\partial x}+\frac{\partial \eta}{\partial x}+\mu^2 V_1+\varepsilon\mu^2 V_2\right\}\mathrm{d}x=0 \tag{3.2}$$

in which w is the weighting function. The third-order spatial derivatives appearing in both (2.3) and (2.4) complicate the situation. If the conventional Galerkin method is used, i.e., the shape function is the same as the weighting function, higher-order finite element approximations, such as the C^1 Hermite cubic polynomial or the C^2 cubic spline, must be employed. This could be computationally expensive for two-dimensional problems. An alternative is to use the Petrov–Galerkin method, in which weighting functions are different from shape functions. To take full advantage of the Petrov–Galerkin method, the weak forms of (3.1) and (3.2) are modified by performing integration by parts. Thus, using (2.3) in (3.1), one obtains

$$\begin{aligned}\int_0^L w\dot{\eta}\,\mathrm{d}x=&\int_0^L\left\{\frac{\partial w}{\partial x}[h+\varepsilon\eta]u_\alpha\right.\\&-\mu^2\left[\frac{\partial w}{\partial x}\left(C_1\frac{\partial h^3}{\partial x}\frac{\partial u_\alpha}{\partial x}+C_3\frac{\partial h^2}{\partial x}\frac{\partial hu_\alpha}{\partial x}\right)+\frac{\partial^2 w}{\partial x^2}\left(C_1h^3\frac{\partial u_\alpha}{\partial x}+C_3h^2\frac{\partial hu_\alpha}{\partial x}\right)\right]\\&-\varepsilon\mu^2\left[\frac{\partial w}{\partial x}\left(C_2\frac{\partial h^2\eta}{\partial x}\frac{\partial u_\alpha}{\partial x}+\beta\frac{\partial h\eta}{\partial x}\frac{\partial hu_\alpha}{\partial x}\right)+\frac{\partial^2 w}{\partial x^2}\left(C_2h^2\eta\frac{\partial u_\alpha}{\partial x}+\beta h\eta\frac{\partial hu_\alpha}{\partial x}\right)\right]\\&\left.+\varepsilon^2\mu^2\left[\frac{\partial w}{\partial x}\left(\frac{1}{2}\frac{\partial \eta^2}{\partial x}\frac{\partial hu_\alpha}{\partial x}\right)+\frac{\partial^2 w}{\partial x^2}\left(\frac{1}{2}\eta^2\frac{\partial hu_\alpha}{\partial x}\right)\right]\right.\end{aligned}$$

$$+\varepsilon^3\mu^2\left[\frac{\partial w}{\partial x}\left(\frac{1}{6}\frac{\partial \eta^3}{\partial x}\frac{\partial u_\alpha}{\partial x}\right)+\frac{\partial^2 w}{\partial x^2}\left(\frac{1}{6}\eta^3\frac{\partial u_\alpha}{\partial x}\right)\right]\Bigg\}\,\mathrm{d}x$$

$$-\Bigg\{w[h+\varepsilon\eta]u_\alpha+\mu^2\left[w\left(C_1h^3\frac{\partial^2 u_\alpha}{\partial x^2}+C_3h^2\frac{\partial^2 hu_\alpha}{\partial x^2}\right)-\frac{\partial w}{\partial x}\left(C_1h^3\frac{\partial u_\alpha}{\partial x}+C_3h^2\frac{\partial hu_\alpha}{\partial x}\right)\right]$$

$$+\varepsilon\mu^2\left[w\left(C_2h^2\eta\frac{\partial^2 u_\alpha}{\partial x^2}+\beta h\eta\frac{\partial^2 hu_\alpha}{\partial x^2}\right)-\frac{\partial w}{\partial x}\left(C_2h^2\eta\frac{\partial u_\alpha}{\partial x}+\beta h\eta\frac{\partial hu_\alpha}{\partial x}\right)\right]$$

$$+\varepsilon^2\mu^2\left[-w\left(\frac{1}{2}\eta^2\frac{\partial^2 hu_\alpha}{\partial x^2}\right)+\frac{\partial w}{\partial x}\left(\frac{1}{2}\eta^2\frac{\partial hu_\alpha}{\partial x}\right)\right]$$

$$+\varepsilon^3\mu^2\left[-w\left(\frac{1}{6}\eta^3\frac{\partial^2 u_\alpha}{\partial x^2}\right)+\frac{\partial w}{\partial x}\left(\frac{1}{6}\eta^3\frac{\partial u_\alpha}{\partial x}\right)\right]\Bigg\}\Bigg|_0^L \tag{3.3}$$

Similarly, (3.2) can be rewritten as

$$\int_0^L\Bigg\{w-\mu^2\left[w\left(C_4\frac{\partial h^2}{\partial x}\frac{\partial}{\partial x}+\beta\left(\frac{\partial h}{\partial x}\right)^2\right)+\frac{\partial w}{\partial x}\left(C_5h^2\frac{\partial}{\partial x}+\frac{\beta}{2}\frac{\partial h^2}{\partial x}\right)\right]$$

$$-\varepsilon\mu^2\left[\frac{\partial w}{\partial x}h\frac{\partial \eta}{\partial x}+\frac{\partial^2 w}{\partial x^2}h\eta\right]-\varepsilon^2\mu^2\left[\frac{1}{2}\frac{\partial w}{\partial x}\frac{\partial \eta^2}{\partial x}+\frac{1}{2}\frac{\partial^2 w}{\partial x^2}\eta^2\right]\Bigg\}\dot{u}_\alpha\,\mathrm{d}x$$

$$=\int_0^L\Bigg\{\frac{\partial w}{\partial x}\left[\eta+\varepsilon\frac{u_\alpha^2}{2}\right]+\varepsilon\mu^2\left[-\frac{\partial w}{\partial x}\left(C_2\frac{\partial h^2u_\alpha}{\partial x}\frac{\partial u_\alpha}{\partial x}+\left(\beta-\frac{1}{2}\right)\left(\frac{\partial hu_\alpha}{\partial x}\right)^2\right)\right.$$

$$\left.-\frac{\partial^2 w}{\partial x^2}\left(\frac{C_2}{2}h^2\frac{\partial u_\alpha^2}{\partial x}+\frac{\beta}{2}\frac{\partial (hu_\alpha)^2}{\partial x}\right)\right]$$

$$+\varepsilon^2\mu^2\left[\frac{\partial w}{\partial x}\left(\frac{\partial \eta u_\alpha}{\partial x}+\eta\frac{\partial u_\alpha}{\partial x}\right)\frac{\partial hu_\alpha}{\partial x}+\frac{\partial^2 w}{\partial x^2}\eta u_\alpha\frac{\partial hu_\alpha}{\partial x}\right]$$

$$+\varepsilon^3\mu^2\left[\frac{1}{2}\frac{\partial w}{\partial x}\left(\frac{\partial \eta^2 u_\alpha}{\partial x}+\eta^2\frac{\partial u_\alpha}{\partial x}\right)\frac{\partial u_\alpha}{\partial x}+\frac{1}{4}\frac{\partial^2 w}{\partial x^2}\eta^2\frac{\partial u_\alpha^2}{\partial x}\right]\Bigg\}\,\mathrm{d}x$$

$$-\Bigg\{w\left[\eta+\varepsilon\frac{u_\alpha^2}{2}\right]+\mu^2w\left[C_2h^2\frac{\partial \dot{u}_\alpha}{\partial x}+\beta h\frac{\partial h\dot{u}_\alpha}{\partial x}\right]$$

$$+\varepsilon\mu^2\left[w\left(\beta hu_\alpha\frac{\partial^2 hu_\alpha}{\partial x^2}+C_2h^2u_\alpha\frac{\partial^2 u_\alpha}{\partial x^2}+\frac{1}{2}\left(\frac{\partial hu_\alpha}{\partial x}\right)^2-\eta\frac{\partial h\dot{u}_\alpha}{\partial x}\right)\right.$$

$$
\begin{aligned}
&- \frac{\partial w}{\partial x}\left(\frac{C_2}{2} h^2 \frac{\partial u_\alpha^2}{\partial x} + \beta h u_\alpha \frac{\partial h u_\alpha}{\partial x} - h\eta \dot{u}_\alpha\right)\Bigg] \\
&+ \varepsilon^2 \mu^2 \Bigg[w\left(- \eta u_\alpha \frac{\partial^2 h u_\alpha}{\partial x^2} + \eta \frac{\partial u_\alpha}{\partial x} \frac{\partial h u_\alpha}{\partial x} - \frac{1}{2}\eta^2 \frac{\partial \dot{u}_\alpha}{\partial x}\right) \\
&+ \frac{\partial w}{\partial x}\left(\eta u_\alpha \frac{\partial h u_\alpha}{\partial x} + \frac{1}{2}\eta^2 \dot{u}_\alpha\right)\Bigg] \\
&+ \varepsilon^3 \mu^2 \Bigg[w\left(- \frac{1}{2}\eta^2 u_\alpha \frac{\partial^2 u_\alpha}{\partial x^2} + \frac{1}{2}\eta^2 \left(\frac{\partial u_\alpha}{\partial x}\right)^2\right) + \frac{\partial w}{\partial x}\left(\frac{1}{4}\eta^2 \frac{\partial u_\alpha^2}{\partial x}\right)\Bigg]\Bigg\}\Bigg|_0^L
\end{aligned}
\tag{3.4}
$$

in which

$$
C_1 = \frac{1}{2}\left(\beta^2 - \frac{1}{3}\right), \quad C_2 = \frac{1}{2}\beta^2, \quad C_3 = \beta + \frac{1}{2}, \quad C_4 = \frac{1}{2}\beta(\beta+1), \quad C_5 = \frac{1}{2}\beta^2 + \beta,
$$
$$
C_6 = \frac{1}{2}\beta^2 + \beta + \frac{1}{3}, \quad \beta = \frac{z_\alpha}{h} \tag{3.5}
$$

and $\dot{u}_\alpha = \partial u_\alpha / \partial t$ and $\dot{\eta} = \partial \eta / \partial t$. Note that in (3.3) and (3.4), the second-order spatial derivatives have been switched from dependent variables, u_α and η, to the weighting function w. Thus, the dependent variables are required to be only once differentiable. In other words, we can now choose the shape function for dependent variables as piecewise linear with C^0 continuity, while the weighting function as piecewise cubic with C^2 continuity.

For spatial approximation, the computational domain is divided into J elements of length $\Delta x_j = x_j - x_{j-1}$, $j = 1, 2, \ldots, J$. The time step size Δt is assumed to be a constant. The dependent variables are represented in the form of a linear combination of shape functions ($\psi_j(x)$), which is now different from the weighting functions ($\phi_j(x)$), and the corresponding nodal values ($\{\eta\}_j^n$, $\{u_\alpha\}_j^n$) as follows:

$$
\eta(x,\ n\Delta t) = \sum_{j=0}^{J} \psi_j(x) \{\eta\}_j^n \tag{3.6a}
$$

$$
u_\alpha(x, n\Delta t) = \sum_{j=0}^{J} \psi_j(x) \{u_\alpha\}_j^n \tag{3.6b}
$$

where $n = 0, 1, 2, \ldots$, representing the time level. The water depth is also approximated with the same set of shape functions, i.e.,

$$
h(x) = \sum_{j=0}^{J} \psi_j(x) \{h\}_j \tag{3.6c}
$$

Substituting (3.6) into the weak forms, (3.3) and (3.4), we obtain the following matrix equations:

$$\sum_{j=0}^{J} [M^{\eta}]_{ij} \{\dot{\eta}\}_j^n = \{f^{\eta}\}_i^n + \{q^{\eta}\}_i^n \tag{3.7}$$

$$\sum_{j=0}^{J} [M^{u}]_{ij}^n \{\dot{u}_{\alpha}\}_i^n = \{f^{u}\}_i^n + \{q^{u}\}_i^n \tag{3.8}$$

in which $i = 0, 1, 2, \ldots, J$. In the above equations, $[M^{\eta}]_{ij}$ and $[M^{u}]_{ij}^n$ are the mass matrices, $\{f^{\eta}\}_i^n$ and $\{f^{u}\}_i^n$ the forcing vectors and $\{q^{\eta}\}_i^n$ and $\{q^{u}\}_i^n$ the boundary vectors. The detailed expressions for these matrices and vectors are given in Appendix A. For the interior elements, the boundary vectors $\{q^{\eta}\}_i^n$ and $\{q^{u}\}_i^n$ vanish because contributions from two adjacent elements cancel each other out. Only at the boundary points, $j = 0$ and J, do non-zero values exist for these boundary vectors. The proper treatment of the boundary conditions will be discussed in a later section.

As shown in Appendix A explicitly, the second derivatives are only required for the weighting functions. Thus, we have chosen the typical linear C^0-type shape function and the cubic B-spline C^2-type weighting function in the following analysis. The one-dimensional cubic B-spline function ϕ_i extends over the interval $[x_{i-2}, x_{i+2}]$ of four neighboring elements with the knot $x = x_i$ as the center. The global shape function (ψ_i) and global weighting function (ϕ_i) are displayed in Figure 1. It is customary to express the element shape function and element weighting function in terms of the local co-ordinate ξ, $(-1 \le \xi \le 1)$, defined over each element in the form

$$\begin{cases} \psi_1^e = \dfrac{1}{2}(1-\xi) \\ \psi_2^e = \dfrac{1}{2}(1-\xi) \end{cases} \tag{3.9a}$$

$$\begin{cases} \phi_1^e = \dfrac{1}{6}\left[\dfrac{1}{8}(1-\xi)^3\right] \\ \phi_2^e = \dfrac{1}{6}\left[1 + \dfrac{3}{2}(1-\xi) + \dfrac{3}{4}(1-\xi)^2 - \dfrac{3}{8}(1-\xi)^3\right] \\ \phi_3^e = \dfrac{1}{6}\left[1 + \dfrac{3}{2}(1+\xi) + \dfrac{3}{4}(1+\xi)^2 - \dfrac{3}{8}(1+\xi)^3\right] \\ \phi_4^e = \dfrac{1}{6}\left[\dfrac{1}{8}(1+\xi)^3\right] \end{cases} \tag{3.9b}$$

The numerical integration is performed using Gauss–Legendre scheme after the global co-ordinate (x) is mapped into the element co-ordinate (ξ).

Using this combination of shape and weighting functions provides several advantages. First, the number of unknown variables and governing equations in the present model is two, which

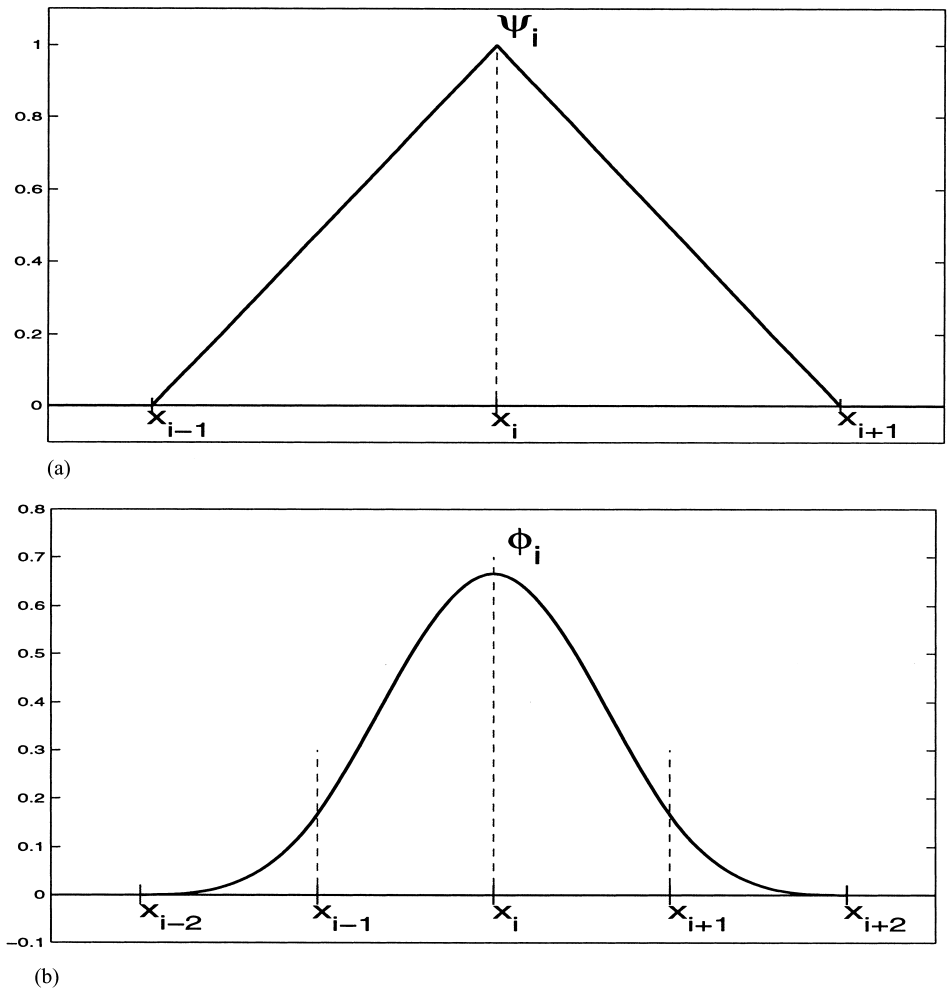

Figure 1. Linear shape function and cubic B-spline weighting function: (a) the global shape function at node i; (b) the global weighting function at node i.

is smaller than that in other FEM models, where auxiliary variables and equations are used. For example, Li *et al.* [14] and Walkley and Berzins [15] need three equations for three unknown variables for weakly non-linear one-dimensional problem. Secondly, the present approach can effectively deal with highly non-linear terms of the order of $O(\varepsilon^2\mu^2)$ and $O(\varepsilon^3\mu^2)$. If we follow Li *et al.*'s [14] approach, those higher-order terms must be expanded in terms of the auxiliary variable, which leads to significant increase in the number of terms in the weak form. On the other hand, if Walkley and Berzins' [15] approach is followed, it is inevitable to introduce one more auxiliary variable to deal with the $O(\varepsilon^2\mu^2)$ and $O(\varepsilon^3\mu^2)$ terms in the

momentum equation, so that there will be four equations for four unknowns. The third advantage is due to the fact that the linear shape function is used in the present Petrov–Galerkin FEM. Compared with the cubic spline Galerkin method, in which the cubic B-spline function is used as a shape function (Gardner and Gardner [21]), the bandwidth of mass matrix ($[M^{\eta}]$, $[M^{u}]$) is reduced. For the one-dimensional problem, the bandwidth is reduced from 7 in the cubic spline Galerkin method to 5 in the present Petrov–Galerkin method. Finally, when the linear shape function is used, it is straightforward to implement the essential boundary condition. In other words, if the dependent variables are known *a priori* at the boundary, nodal values at that point are directly determined from the known dependent variables. However, when cubic B-spline shape function is used, nodal values at the boundary are not clearly determined by the known physical variables.

3.2. Time integration scheme

In this section, we shall describe the Adams–Bashforth–Moulton predictor–corrector scheme to integrate (3.7) and (3.8). For the predictor step, the third-order Adams–Bashforth scheme is employed

$$P[\eta]:\ [M^{\eta}]_{ij}\left(\frac{\{\eta\}_{j(0)}^{n+1}-\{\eta\}_{j}^{n}}{\Delta t}\right)=\frac{1}{12}\left[23\{f^{\eta}\}_{i}^{n}-16\{f^{\eta}\}_{i}^{n-1}+5\{f^{\eta}\}_{i}^{n-2}\right] \tag{3.10}$$

$$P[u_{\alpha}]:\ [M^{u}]_{ij}^{n}\left(\frac{\{u_{\alpha}\}_{j(0)}^{n+1}-\{u_{\alpha}\}_{j}^{n}}{\Delta t}\right)=\frac{1}{12}\left[23\{f^{u}\}_{i}^{n}-16\ \{f^{u}\}_{i}^{n-1}+5\{f^{u}\}_{i}^{n-2}\right] \tag{3.11}$$

Solving the above equations, one obtains solutions for the first predicted values, $\{\eta\}_{j(0)}^{n+1}$ and $\{u_{\alpha}\}_{j(0)}^{n+1}$ at the jth node and $(n+1)$th time step. Using these values, the forcing vectors and the mass matrix are updated at the $(n+1)$th time level; i.e., $\{f^{\eta}\}_{i(0)}^{n+1}$, $\{f^{u}\}_{i(0)}^{n+1}$, $[\tilde{M}_{1}^{u}]_{ij(0)}^{n+1}$, $[\tilde{M}_{2}^{u}]_{ij(0)}^{n+1}$.

The corrected solutions are then obtained by applying the fourth-order Adams–Moulton corrector method. The subsequent iteration procedure can be explained as follows. To obtain the sth corrected value for $\{\eta\}_{j(s)}^{n+1}$, in which s denotes the number of iteration ($s=1, 2, \ldots$), the continuity equation (3.7) is integrated in the following manner:

$$C[\eta]:\ \{\eta\}_{j(s)}^{n+1}=\{\eta\}_{j}^{n}+\frac{\Delta t}{24}[M^{\eta}]_{ij}^{-1}(9\{f^{\eta}\}_{i(s-1)}^{n+1}+19\{f^{\eta}\}_{i}^{n}-5\{f^{\eta}\}_{i}^{n-1}+\{f^{\eta}\}_{i}^{n-2}) \tag{3.12}$$

Using $\{\eta\}_{j(s)}^{n+1}$ and $\{u_{\alpha}\}_{j(s-1)}^{n+1}$, we update the forcing vector $\{f^{u}\}_{i(s-1)}^{n+1}$ and the mass matrix $[\tilde{M}_{1}^{u}]_{ij(s-1)}^{n+1}$, $[\tilde{M}_{2}^{u}]_{ij(s-1)}^{n+1}$. The momentum equation (3.8) can be integrated as

$$C[u_{\alpha}]:\ \{u_{\alpha}\}_{j(s)}^{n+1}=\{u_{\alpha}\}_{j}^{n}+\frac{\Delta t}{24}[[M^{u}]_{ij(s-1)}^{n+1}]^{-1}(9\{f^{u}\}_{i(s-1)}^{n+1}+19\{f^{u}\}_{i}^{n}-5\{f^{u}\}_{i}^{n-1}+\{f^{u}\}_{i}^{n-2}) \tag{3.13}$$

The relative errors between two successive correction steps are defined as

$$\Delta e_\eta = \max\left(\frac{\{\eta\}_{j(s)}^{n+1} - \{\eta\}_{j(s-1)}^{n+1}}{\{\eta\}_{j(s)}^{n+1}}\right) \tag{3.14a}$$

$$\Delta e_u = \max\left(\frac{\{u_\alpha\}_{j(s)}^{n+1} - \{u_\alpha\}_{j(s-1)}^{n+1}}{\{u_\alpha\}_{j(s)}^{n+1}}\right) \tag{3.14b}$$

The corrector step continues until both Δe_u and Δe_η are less than 10^{-4}.

3.3. Truncation error analysis

Since third-order spatial derivatives appear in both governing equations, any sensible numerical scheme should be at lest fourth-order accurate in space. In this section, we examine the leading order truncation error of the proposed scheme, following the accuracy analysis suggested by Sanz-Serna and Christie [16]. To simplify the analysis, we focus on the linearized version of the governing equations (2.3) and (2.4) with a constant water depth, i.e.

$$L^\eta \equiv \frac{\partial \eta}{\partial t} + h\frac{\partial u_\alpha}{\partial x} + \mu^2 K_1 \frac{\partial^3 u_\alpha}{\partial x^3} = 0 \tag{3.15}$$

$$L^u \equiv \frac{\partial u_\alpha}{\partial t} + h\frac{\partial \eta}{\partial x} + \mu^2 K_2 \frac{\partial^3 u_\alpha}{\partial t\,\partial x^2} = 0 \tag{3.16}$$

where

$$K_1 = C_6 h^3, \qquad K_2 = C_5 h^2 \tag{3.17}$$

β, C_5 and C_6 have been defined in (3.5). Applying the Petrov–Galerkin scheme as described in Section 3.1 with linear shape functions and cubic B-spline weighting functions to (3.15) and (3.16), we obtain the following equations at an internal node j:

$$\begin{aligned}\tilde{L}^\eta \equiv{}& \frac{1}{120}(\{\dot\eta\}_{j+2} + 26\{\dot\eta\}_{j+1} + 66\{\dot\eta\}_j + 26\{\dot\eta\}_{j-1} + \{\dot\eta\}_{j-2}) \\ &+ \frac{h}{24\Delta x}(\{u_\alpha\}_{j+2} + 10\{u_\alpha\}_{j+1} - 10\{u_\alpha\}_{j-1} - \{u_\alpha\}_{j-2}) \\ &+ \mu^2 \frac{K_1}{2(\Delta x)^3}(\{u_\alpha\}_{j+2} - 2\{u_\alpha\}_{j+1} + 2\{u_\alpha\}_{j-1} - \{u_\alpha\}_{j-2}) = 0\end{aligned} \tag{3.18}$$

$$\begin{aligned}\tilde{L}^u \equiv{}& \frac{1}{120}(\{\dot u_\alpha\}_{j+2} + 26\{\dot u_\alpha\}_{j+1} + 66\{\dot u_\alpha\}_j + 26\{\dot u_\alpha\}_{j-1} + \{\dot u_\alpha\}_{j-2}) \\ &+ \frac{h}{24\Delta x}(\{\eta\}_{j+2} + 10\{\eta\}_{j+1} - 10\{\eta\}_{j-1} - \{\eta\}_{j-2}) \\ &+ \mu^2 \frac{K_2}{6(\Delta x)^2}(\{\dot u_\alpha\}_{j+2} + 2\{\dot u_\alpha\}_{j+1} - 6\{\dot u_\alpha\}_j + 2\{\dot u_\alpha\}_{j-1} + \{\dot u_\alpha\}_{j-2}) = 0\end{aligned} \tag{3.19}$$

in which Δx is the uniform element size. We remark here that (3.18) and (3.19) are subsets of (3.7) and (3.8), in which the non-linear terms, varying water depth and the boundary effects are all excluded.

Using the Taylor series expansions in space, we can rewrite (3.18) and (3.19) in the following forms:

$$\tilde{L}^{\eta} = L^{\eta} + \frac{(\Delta x)^2}{4}\frac{\partial^2}{\partial x^2}(L^{\eta}) + (\Delta x)^4\left\{\frac{7}{240}\frac{\partial^4 \dot{\eta}}{\partial x^4} + \frac{7h}{240}\frac{\partial^5 u_{\alpha}}{\partial x^5} + \mu^2\frac{K_1}{40}\frac{\partial^7 u_{\alpha}}{\partial x^7}\right\} + O(\Delta x)^6 \tag{3.20}$$

$$\tilde{L}^{u} = L^{u} + \frac{(\Delta x)^2}{4}\frac{\partial^2}{\partial x^2}(L^{u}) + (\Delta x)^4\left\{\frac{7}{240}\frac{\partial^4 \dot{u}_{\alpha}}{\partial x^4} + \frac{7}{240}\frac{\partial^5 \eta}{\partial x^5} + \mu^2\frac{11K_2}{360}\frac{\partial^6 u_{\alpha}}{\partial x^6}\right\} + O(\Delta x)^6 \tag{3.21}$$

The modified partial differential equations (PDEs), $\tilde{L}^{\eta} = 0$ and $\tilde{L}^{u} = 0$, are different from the original PDEs, $L^{\eta} = 0$ and $L^{u} = 0$. The leading truncation error is of $O(\Delta x)^4$. Also, note that the leading truncation error is in the form of fourth-order spatial derivative. Therefore, the frequency dispersive behavior in the governing equations, which are represented by the second- and third-order spatial derivative terms, is not significantly affected by the numerical error.

3.4. Stability analysis

A Von Neumann stability analysis has been performed for the proposed time integration scheme. Once again the analysis is only applicable to the linearized version of the governing equations with a constant depth. Assuming that the solutions at the time step, $n\Delta t$ and the jth node can be expressed in terms of a Fourier component as

$$\{\eta\}_j^n = \eta_0 \xi^n \, \mathrm{e}^{\hat{\mathrm{i}}\kappa(j\Delta x)} \tag{3.22a}$$

$$\{u_{\alpha}\}_j^n = u_0 \xi^n \, \mathrm{e}^{\hat{\mathrm{i}}k(j\Delta x)} \tag{3.22b}$$

where η_0 and u_0 are the amplitudes of the Fourier component for η and u_{α}, respectively, ξ is the amplification factor, κ the wave number of the Fourier component and $\hat{\mathrm{i}}$ the imaginary constant. By substituting (3.22) into the numerical scheme for the predictor step, i.e., (3.10) and (3.11), we can find the relationship between (η_0, u_0) and $(\{\eta\}_{j(0)}^{n+1}, \{u_{\alpha}\}_{j(0)}^{n+1})$

$$\{\eta\}_{j(0)}^{n+1} = [\xi^2\eta_0 + D_4(23\xi^2 - 16\xi + 5)u_0]\xi^{n-2} \, \mathrm{e}^{\hat{\mathrm{i}}\kappa(j\Delta x)} \tag{3.23a}$$

$$\{u_{\alpha}\}_{j(0)}^{n+1} = [D_5(23\xi^2 - 16\xi + 5)\eta_0 + \xi^2 u_0]\xi^{n-2} \, \mathrm{e}^{\hat{\mathrm{i}}\kappa(j\Delta x)} \tag{3.23b}$$

in which

$$D_0 = \frac{1}{60}[\cos(2\kappa\Delta x) + 26\cos(\kappa\Delta x) + 33] \tag{3.24a}$$

$$D_1 = \frac{\hat{\mathrm{i}}}{12\Delta x}\left[\sin(2\kappa\Delta x) + 10\sin(\kappa\Delta x)\right] \tag{3.24b}$$

$$D_2 = \frac{1}{6\Delta x}\left[\cos(2\kappa\Delta x) + 2\cos(\kappa\Delta x) - 3\right] \tag{3.24c}$$

$$D_3 = \frac{\hat{\mathrm{i}}}{(\Delta x)^3}\left[(\sin(2\kappa\Delta x) - 2\sin(\kappa\Delta x)\right] \tag{3.24d}$$

$$D_4 = -\frac{\Delta t}{12}\left(\frac{hD_1 + \mu^2 K_1 D_3}{D_0}\right) \tag{3.24e}$$

$$D_5 = -\frac{\Delta t}{12}\left(\frac{D_1}{D_0 + \mu^2 K_2 D_2}\right) \tag{3.24f}$$

For the first corrector step ($s = 1$ in (3.12) and (3.13)), the above expressions are used for evaluating $\{f^{\eta}\}_{j(0)}^{n+1}$ and $\{f^{u}\}_{j(0)}^{n+1}$. We obtain the relationships between (η_0, u_0) and $(\{\eta\}_{j(1)}^{n+1}, \{u_\alpha\}_{j(1)}^{n+1})$

$$\{\eta\}_{j(1)}^{n+1} = \left\{\left[\xi^2 + \frac{9}{2}D_4 D_5(23\xi^2 - 16\xi + 5)\right]\eta_0 + \frac{D_4}{2}[9\xi^2 + 19\xi^2 - 5\xi + 1]u_0\right\}\xi^{n-2}\,\mathrm{e}^{\hat{\mathrm{i}}\kappa(j\Delta x)} \tag{3.25a}$$

$$\{u_\alpha\}_{j(1)}^{n+1} = \left\{\frac{D^5}{2}[9\xi^2 + 19\xi^2 - 5\xi + 1]\eta_0 + \left[\xi^2 + \frac{9}{2}D_4 D_5(23\xi^2 - 16\xi + 5)\right]u_0\right\}\xi^{n-2}\,\mathrm{e}^{\hat{\mathrm{i}}\kappa(j\Delta x)} \tag{3.25b}$$

Repeating the procedure for the successive corrector step, we can construct relationships between (η_0, u_0) and $(\{\eta\}_{j(s)}^{n+1}, \{u_\alpha\}_{j(s)}^{n+1})$. Finally, we replace $\{\eta\}_{j(s)}^{n+1}$ and $\{u_\alpha\}_{j(s)}^{n+1}$ by the Fourier component forms as shown in (3.22). This leads to a 2×2 homogeneous matrix equation for (η_0, u_0). The determinant of the matrix equation, which is a sixth degree polynomial in ξ, must be zero for non-trivial solutions for u_0 and η_0. The amplification factor ξ, which is assumed to be a complex quantity, can be found by solving the resulting equation numerically. We remark here that in the resulting equation for ξ there are three free parameters, $\kappa\Delta x$, Courant number $Cr = \sqrt{gh}\Delta t/\Delta x$ and $\Delta x/h$. Moreover, the precise expression of the equation depends on the number of iterations.

Some of the results for the amplification factor are shown in Figure 2. By using $Cr = 1$ and $\Delta x/h = 0.2$, Figure 2(a) shows the variation of the largest modulus of the amplification factor at different iteration step as a function of $\kappa\Delta x$. The notation 1st in the figure denotes the first corrector step. In other words, the predictor step is always performed first. The upper bound of the abscissa represents the wave component with wavelength of $2\Delta x$. The amplification factor approaches unity rapidly from the first corrector step to second corrector step. At third corrector step, the amplification factor is slightly bigger than unity in the intermediate wave range and this feature does not change up to the ninth iteration corrector step, at which the

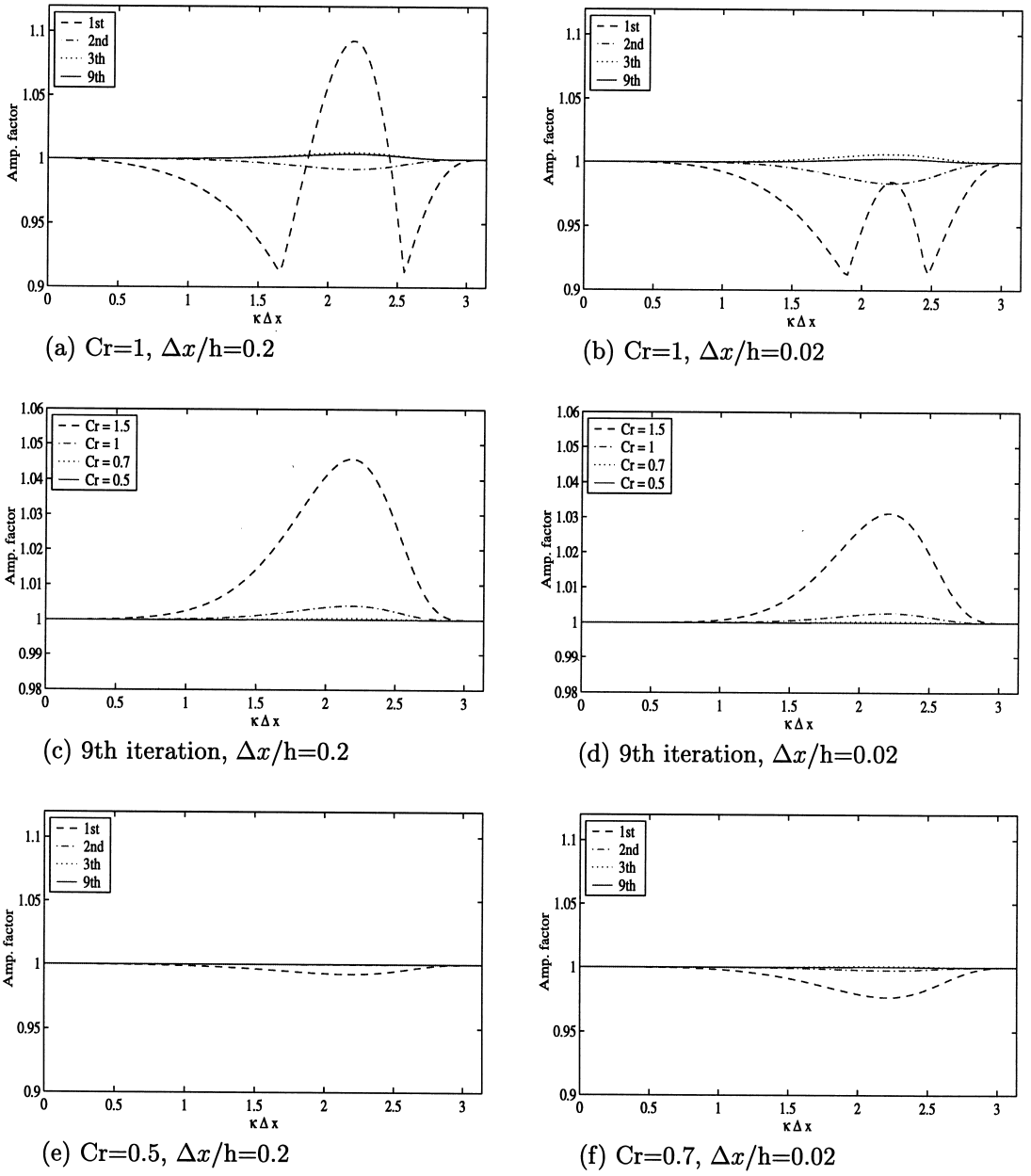

Figure 2. The amplification factor at different iteration and Courant number.

maximum $\xi = 1.004$ occurs at $\kappa\Delta x = 2.175$. By reducing the element size to $\Delta x/h = 0.02$, the stability of the first corrector improved (Figure 2(b)). However, the overall variation of amplification factor in terms of number of iteration is not affected much.

For various Courant numbers, the amplification factor of the ninth iteration is shown in Figure 2(c) and (d). The numerical scheme is stable as long as the Courant number is less than 0.5 and if nine iterations are performed at each different time step. The difference of the maximum amplification factor at $Cr = 0.7$ and 0.5 is just 0.03 per cent. Figure 2(e) and (f) shows the variation of the amplification factor in terms of iteration number at different Courant number and element size, which assures our stability criteria.

3.5. Boundary conditions

Appropriate boundary conditions are needed to obtain proper numerical solutions for wave propagation in a finite computational domain. Here, we shall discuss two kinds of boundary conditions, i.e., an incident wave boundary condition and the perfect reflecting boundary condition.

3.5.1. Incident wave boundary condition. At the incident wave boundary, the time series of η and u are known. Since the nodal value at the boundary is known, it is regarded as an essential boundary condition. The following procedure is used to implement the boundary condition in the Petrov–Galerkin method with the implicit time integration scheme.

Suppose that the time histories of η and u at node number m are given. As shown in the previous section, Equation (3.7) is solved for $\{\eta\}_j^{n+1}$. Since $\{\eta\}_{j=m}^{n+1}$ is known, the matrix $[M^\eta]_{ij}$ and vector $\{f^\eta\}_i^n$ should be modified. Specifically, the elements of the mth row of $[M^\eta]$ are set to zero, except for the element $[M^\eta]_{mm}$, which is set to unity. The mth row of the vector $\{f^\eta\}_{i=m}^n$ is also replaced by the following known information:

$$\{f^\eta\}_m^n = \left(\frac{\{\eta\}_m^{n+1}* - \{\eta\}_m^n}{\Delta t}\right) \tag{3.26}$$

where $\{\eta\}_m^{n+1}*$ is the known value at next time step. For the predictor step of continuity equation (3.10), the mth row of the matrix equation becomes

$$[0 \quad 0 \quad \cdots \quad 1 \quad \cdots \quad 0 \quad 0]\left(\frac{\{\eta\}_{m(0)}^{n+1} - \{\eta\}_m^n}{\Delta t}\right) = \left(\frac{\{\eta\}_m^{n+1}* - \{\eta\}_m^n}{\Delta t}\right) \tag{3.27}$$

in which the '1' locates at mth column. Consequently, the boundary condition for $\{\eta\}_m^{n+1}$ has been applied. The same approach is applied to the momentum equations and the subsequent iterative corrector procedure.

If the incident wave boundary is located at the left-hand side of the computational domain, the given surface elevation and velocities are assigned to nodal values at $j = 0$ and 1. The solution at node $j = 2$, where the real computational domain begins, depends on these two nodal values. Because the weighting function is distributed over four elements (five nodes, see Figure 1(b)), nodal values at $j = 0$, 1 are coupled with the nodal value at $j = 2$. We should remark here that imposing two adjacent Dirichlet conditions is similar to specifying a first

spatial derivative at the boundary. This may lead to difficulties for non-linear wave input, similar to those encountered from imposing solution and its derivative at a single point. However, by increasing the number of nodes where the Dirichlet conditions are applied, we can increase, in principle, the accuracy of spatial derivative at the boundary.

3.5.2. Reflective wall boundary. To satisfy the no-flux boundary condition approximately, the depth-averaged velocity, $\bar{u}$, must vanish. Since the relationship between $\bar{u}$ and u_α can be rewritten as

$$\bar{u} = u_\alpha + \frac{\mu^2}{2}(z_\alpha^2 - z^2)\frac{\partial^2 u_\alpha}{\partial x^2} + \mu^2(z_\alpha - z)\frac{\partial^2 h u_\alpha}{\partial x^2} \tag{3.28}$$

both u_α and $\partial^2 u_\alpha/\partial x^2$ must be zero under the assumption of constant depth near the boundary. The normal gradient of surface elevation is also zero up to the leading order of the Boussinesq approximation. These conditions can be implemented by the method of image.

Suppose that the node at $j = J-2$ is the wall boundary. Therefore, the following is true:

$$\{u_\alpha\}_{J-2} = 0 \tag{3.29a}$$

$$\{u_\alpha\}_{J-1} = -\{u_\alpha\}_{J-3} \tag{3.29b}$$

$$\{u_\alpha\}_{J} = -\{u_\alpha\}_{J-4} \tag{3.29c}$$

$$\{\eta\}_{J-1} = \{\eta\}_{J-3} \tag{3.29d}$$

$$\{\eta\}_{J} = \{\eta\}_{J-4} \tag{3.29e}$$

We can apply the essential boundary condition for $\{u_\alpha\}_{J-2}$ and the natural boundary condition for $\{\eta\}_{J-2}$. To satisfy the natural boundary condition for $\{\eta\}_{J-2}$, we treat two additional nodes $j = J-1$, J as essential boundary condition. We can solve for $\{\eta\}_{J-2}$.

The general procedure for dealing with the essential boundary condition is similar to the incident wave boundary condition discussed in the previous section, except the fact that now the nodal value where the essential boundary is applied is not known *a priori*. They should be solved together with the prescribed condition.

If we apply the iterative (implicit) time integration scheme, the boundary conditions indicated above can be dealt with in such a way that (after modifying the matrix for the corresponding row)

$$[M^u]^n_{J-2\,j}\left(\frac{\{u_\alpha\}^{n+1}_{J-2(s)} - \{u_\alpha\}^n_{J-2}}{\Delta t}\right) = \{f^u\}^n_{J-2} = \left(\frac{0 - \{u_\alpha\}^n_{J-2}}{\Delta t}\right) \tag{3.30a}$$

$$[M^u]^n_{J-1\,j}\left(\frac{\{u_\alpha\}^{n+1}_{J-1(s)} - \{u_\alpha\}^n_{J-1}}{\Delta t}\right) = \{f^u\}^n_{J-1} = \left(\frac{-\{u_\alpha\}^{n+1}_{J-3(s-1)} - \{u_\alpha\}^n_{J-1}}{\Delta t}\right) \tag{3.30b}$$

$$[M^u]^n_{J\ j}\left(\frac{\{u_\alpha\}^{n+1}_{J(s)}-\{u_\alpha\}^n_J}{\Delta t}\right)=\{f^u\}^n_J=\left(\frac{-\{u_\alpha\}^{n+1}_{J-4(s-1)}-\{u_\alpha\}^n_J}{\Delta t}\right) \tag{3.30c}$$

$$[M^\eta]^n_{J-1\ j}\left(\frac{\{\eta\}^{n+1}_{J-1(s)}-\{\eta\}^n_{J-1}}{\Delta t}\right)=\{f^\eta\}^n_{J-1}=\left(\frac{\{\eta\}^{n+1}_{J-3(s-1)}-\{\eta\}^n_{J-1}}{\Delta t}\right) \tag{3.30d}$$

$$[M^\eta]^n_{J\ j}\left(\frac{\{\eta\}^{n+1}_{J(s)}-\{\eta\}^n_J}{\Delta t}\right)=\{f^\eta\}^n_J=\left(\frac{\{\eta\}^{n+1}_{J-4(s-1)}-\{\eta\}^n_J}{\Delta t}\right) \tag{3.30e}$$

where Equations (3.30a)–(3.30e) represent the conditions described in Equations (3.29a)–(3.29e) respectively.

4. NUMERICAL RESULTS

4.1. Solitary wave propagation over constant depth

The small amplitude solitary wave can propagate over a long distance without changing shape. The present numerical scheme is first tested for this case. To avoid potential complications caused by the boundary conditions, the theoretical surface profile and the corresponding velocity field for a solitary wave are used as the initial conditions.

The approximate solitary wave solution of Nwogu's [20] extended Boussinesq equations was derived by Wei and Kirby [6]

$$\eta = A_1\,\mathrm{sech}^2[B(x-\tilde{c}t)] + A_2\,\mathrm{sech}^4[B(x-\tilde{c}t)] \tag{4.1}$$

$$u = A\,\mathrm{sech}^2[B(x-\tilde{c}t)] \tag{4.2}$$

where

$$\tilde{c}=\sqrt{(gh_0)}c \tag{4.3a}$$

$$A_1=\frac{h_0}{3}\left(\frac{c^2-1}{C_6-C_5c^2}\right) \tag{4.3b}$$

$$A_2=-\frac{h_0}{2}\left(\frac{c^2-1}{c}\right)^2\left(\frac{C_6+C_5c^2}{C_6-C_5c^2}\right) \tag{4.3c}$$

$$A=\sqrt{gh_0}\left(\frac{c^2-1}{c}\right) \tag{4.3d}$$

$$B=\frac{1}{2h_0}\sqrt{\left(\frac{c^2-1}{C_6-C_5c^2}\right)} \tag{4.3e}$$

The parameter c is decided by solving

$$2C_5(c^2)^3 - \left(3C_5 + \frac{1}{3} + 2\epsilon C_5\right)(c^2)^2 + 2\epsilon C_6(c^2) + C_6 = 0 \tag{4.3f}$$

The computational domain is made large enough so that both the free surface displacement and the velocity vanish at the boundary throughout the entire numerical simulation. Figure 3(a) shows a snap shot of the solitary wave with amplitude 0.1 m over constant depth of 1 m. The crest of the initial solitary wave is located at $x = 0$. Therefore, at the moment shown in Figure 3, the wave has traveled a distance close to one thousand water depths. In the numerical computations $\Delta x = 0.4$ m and $\Delta t = 0.06$ s are used. The 'wavelength', λ, is defined as the width under the solitary wave where $\eta/h_0 \geq 0.001$ (Goring [22]). It is estimated as 30.3

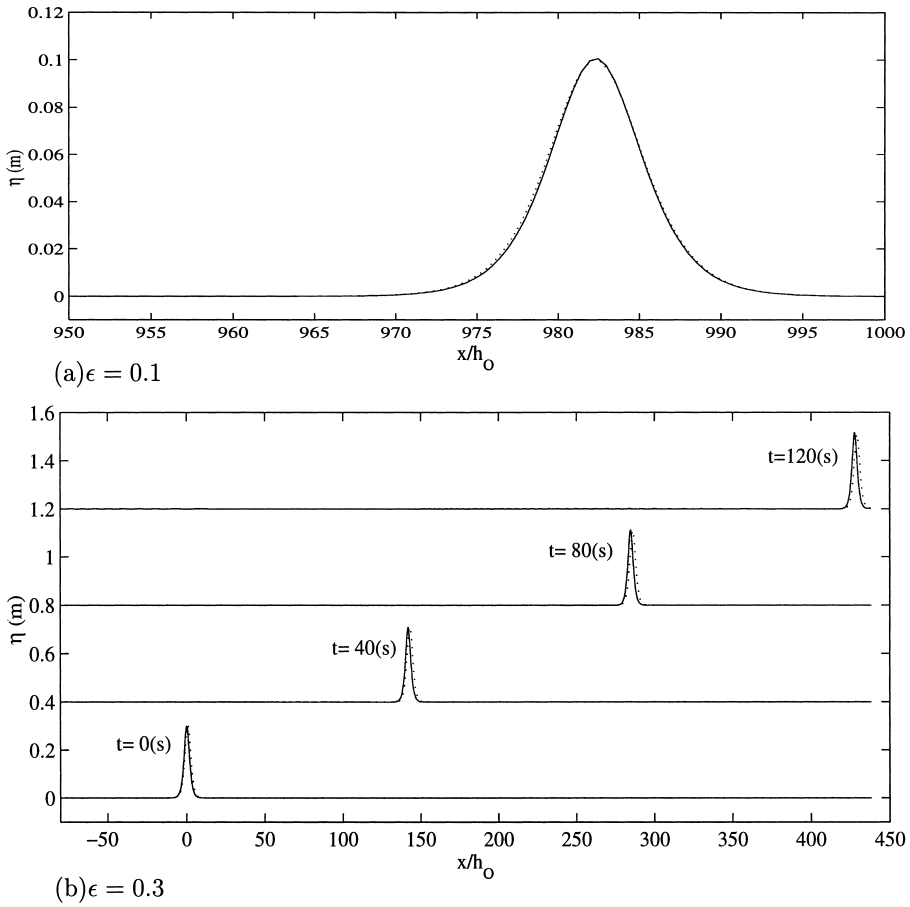

Figure 3. Solitary wave propagation over constant depth: — present numerical result; - - - analytical solution.

m and the corresponding 'wave period' (T) is calculated from the linear dispersion relation as 9.2 s. There are about 75 elements within the solitary wave. Because the wave amplitude is quite small, the numerical results are almost identical to the theoretical solution, which is also plotted in Figure 3(a).

For a larger solitary wave with 0.3 m amplitude, a slight phase error appears (Figure 3(b)). The phase speed is slightly smaller than the theoretical one and the maximum amplitude is also slightly overpredicted. This result agrees with other numerical solutions [6,14,15].

If the initial wave amplitude of the solitary wave is increased to 0.6 m ($\epsilon = 0.6$) in the numerical simulation, a small oscillatory tail develops behind the main wave and the wave height increases by 10 per cent at the beginning of the computation. The oscillatory tails appear because the analytical solution for solitary wave, given in (4.1) and (4.2), is no longer valid for such a large wave amplitude. The numerical model adjusts the mismatch between the initial conditions and the model equations and finally produces a permanent-form solitary wave-like solution. This numerical solitary wave solution is compared with those of different numerical models with different governing equations (Figure 4). These models include the boundary element method (BEM) for a fully non-linear potential flow [23], the finite difference method (FDM) of extended Boussinesq equations [20], and the finite difference method of fully non-linear and weakly dispersive equations [2]. The calculated results from other numerical models are obtained by digitizing the plots presented in Wei *et al*. [2]. The present finite element solutions are very close to those of other numerical models.

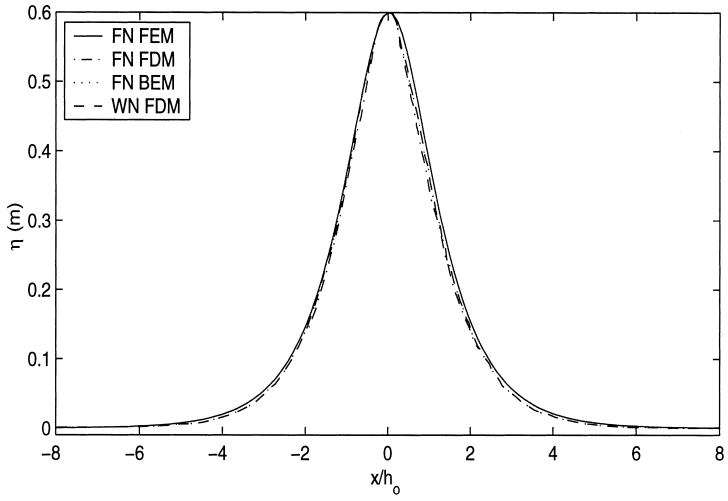

Figure 4. Comparison of different numerical solutions for solitary wave with $\epsilon = 0.6$. FN FEM: fully non-linear Boussinesq FEM; FN FDM: fully non-linear Boussinesq FDM [2]; FN BEM: fully non-linear potential flow BEM [23]; WN FDM: weakly non-linear FDM [20].

4.2. Solitary wave shoaling on slopes

Numerical simulations for the shoaling of a non-breaking solitary wave over plane slope are performed. Through this analysis, the non-linear portion of the present numerical model can be examined. The test case chosen here is the same as the one studied by Wei *et al.* [2].

The crest of the initial solitary wave is located at $x = 0$, where the beach slope (1:35) begins. The water depth is 0.71 m at $x/h_0 = 10$ and 0.2 m at $x/h_0 = 28$. The incident wave height is $\epsilon = 0.2$. In numerical computations, $T/\mathrm{d}t = 150$ and $\lambda/\Delta x = 80$ are used. As shown in Figure 5, the present numerical solutions agree well with those of other fully non-linear models in terms of wave amplitude and the free surface shape. The dimensionless time (t') and co-ordinate (x') have been scaled by $\sqrt{(h_0/g)}$ and h_0 respectively.

When $t' = t_3$, the maximum relative wave height, $\epsilon_{\max}$ $(= a_{\max}/h)$ is 1.06. The present numerical results reach $\epsilon_{\max} = 1.4$, a theoretical breaking index [24] at $t' = 25.36$ and $x' = 25.5$, which is slightly earlier than $t' = 25.94$ and $x' = 25.9$, as suggested by Wei *et al.* [2]. After the solitary wave passes this point, wiggles starts to emerge at the crest. At $t' = t_4 = 25.93$, the present numerical wave form shows small discontinuity.

4.3. Fission of solitary wave

It has been found theoretically and experimentally that a solitary wave, traveling from one constant depth to another smaller constant depth, disintegrates into several solitons of different sizes, which is called the fission phenomenon. Figure 6 shows the evolution of a solitary wave propagating over a slope onto a shallower depth. The numerical results are calculated using $T/\mathrm{d}t = 100$ and $\lambda/\Delta x = 50$. The ϵ of the incoming wave at $x/h_0 = 0$ is 0.12 and

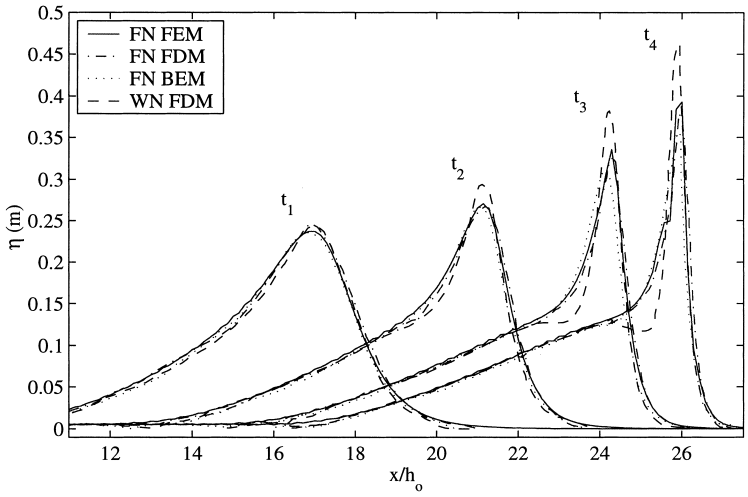

Figure 5. Comparison of spatial profile of solitary wave shoaling on 1:35 slope with $\epsilon = 0.2$ at different time step ($t' = t_1 = 16.24$, $t_2 = 20.64$, $t_3 = 24.03$, $t_4 = 25.93$). See Figure 4 for abreviations.

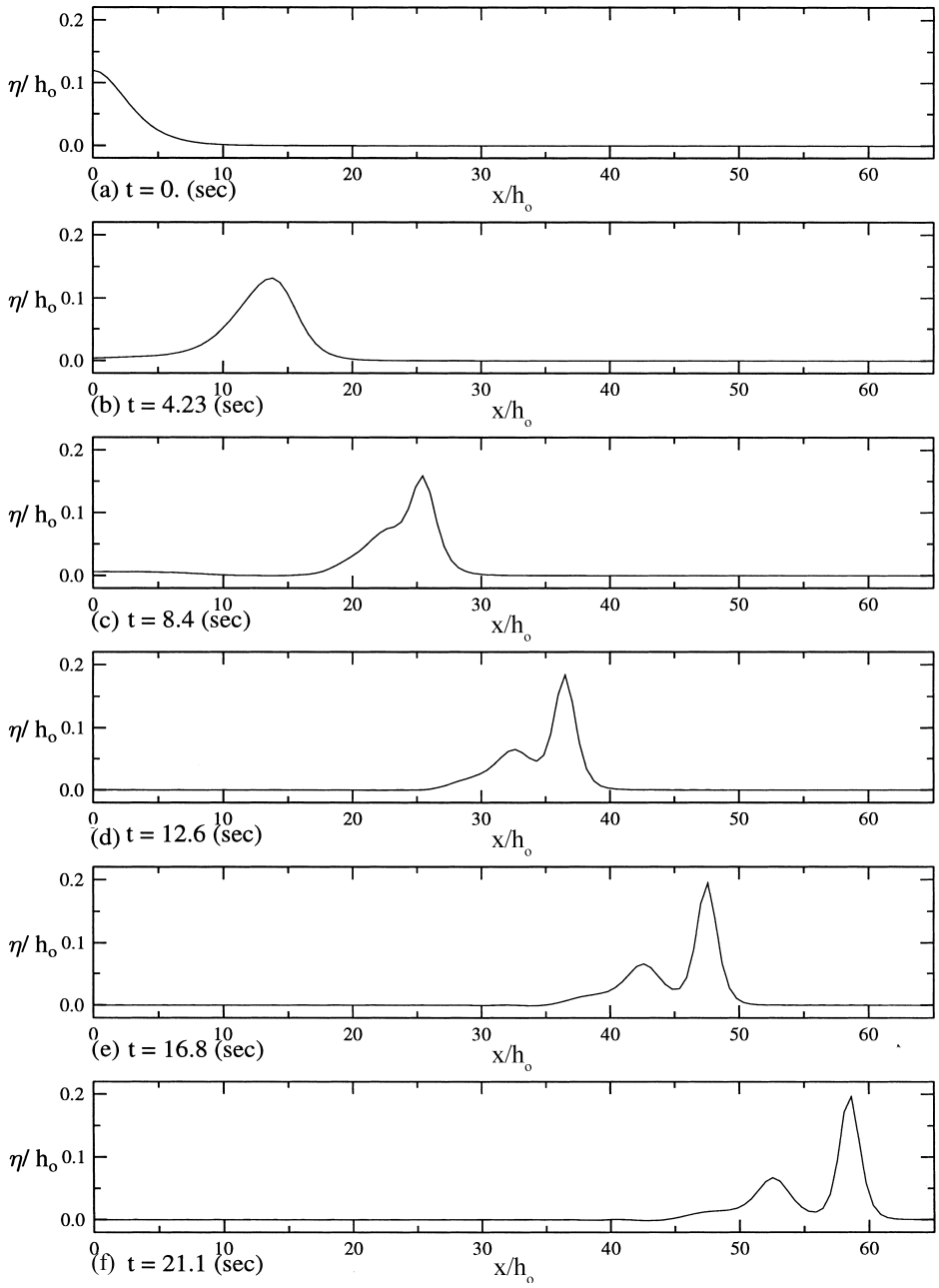

Figure 6. Fission of a solitary wave propagating over an 1:20 slope onto a shallower depth.

the varying depth exists from $x/h_0 = 10$ to $x/h_0 = 15$, with the slope of 1:20. The fission process is well demonstrated. In Figure 7, the numerical results of the present model are compared with those of Navier–Stokes equations model [25]. Agreement among the numerical results is excellent.

4.4. Propagation of deep water wave

A numerical experiment is performed to evaluate the ability of simulating the propagation of periodic waves in deep water. The sinusoidal wave with wavelength 2 m and waveheight 0.1 m is given as an initial condition over the constant water depth of 1 m. The rightmost 1/4 wavelength of the initial condition are tapered off using $a\ \mathrm{sech}^2(0.5kx)$ to avoid the abrupt changes of the water surface at the edge. Since $kh = 3.14$ in this case, the conventional Boussinesq equations are not the appropriate model for its dispersion relation does not converge if $kh > 3.016$.

Figure 8 shows the spatial profiles of the propagating waves at different instances. The vertical line denotes the location of a wave crest at different times according to the exact phase speed calculated from the linear dispersion relationship. The phase speed of the present model agrees very well with the exact phase speed.

4.5. Wave–wave interaction

By simulating the collision of two solitary waves propagating in opposite directions, the capability of the numerical model in dealing with non-linear wave–wave interactions can be tested. Two identical solitary waves with $\epsilon = 0.6$ are introduced in a constant water depth (see Figure 9). In the computations, $T/\mathrm{d}t = 120$ and $\lambda/\Delta x = 70$ are used. As mentioned before, because of the inadequacy of the solutions to describe the large solitary wave, small oscillatory tails are generated initially. After these tails are separated from the numerically generated solitary wave, the process of collision and passing of two solitary waves is well represented.

4.6. Applications of the boundary conditions

The incident wave boundary and the perfect reflecting wall boundary condition are implemented in a simple wave tank. First, a solitary wave of amplitude 0.1 m over the constant water depth of 1 m is generated through the left-hand boundary and is reflected totally from the right-hand boundary. In the computations $T/\mathrm{d}t = 120$ and $\lambda/\Delta x = 70$ are used (Figure 10). The numerical results show that the numerical schemes for the incident wave boundary and reflective wall boundary perform well for solitary wave of $\epsilon = 0.1$.

To check further the accuracy of the reflected wall boundary condition, a solitary wave is set free to propagate between two perfectly reflecting walls. The initial solitary wave of $\epsilon = 0.1$ is given with the crest at $x/h_0 = 0$. The computational domain is $-17 \le x/h_0 \le 17$. The time history of the free surface elevation and velocity at the center of the tank ($x/h_0 = 0$) are plotted in Figure 11. The computations were performed up to 40 wave periods, during which time the wave has moved forward and backward seven times. The maximum amplitude and velocity at different period remain almost constant over the whole computational period.

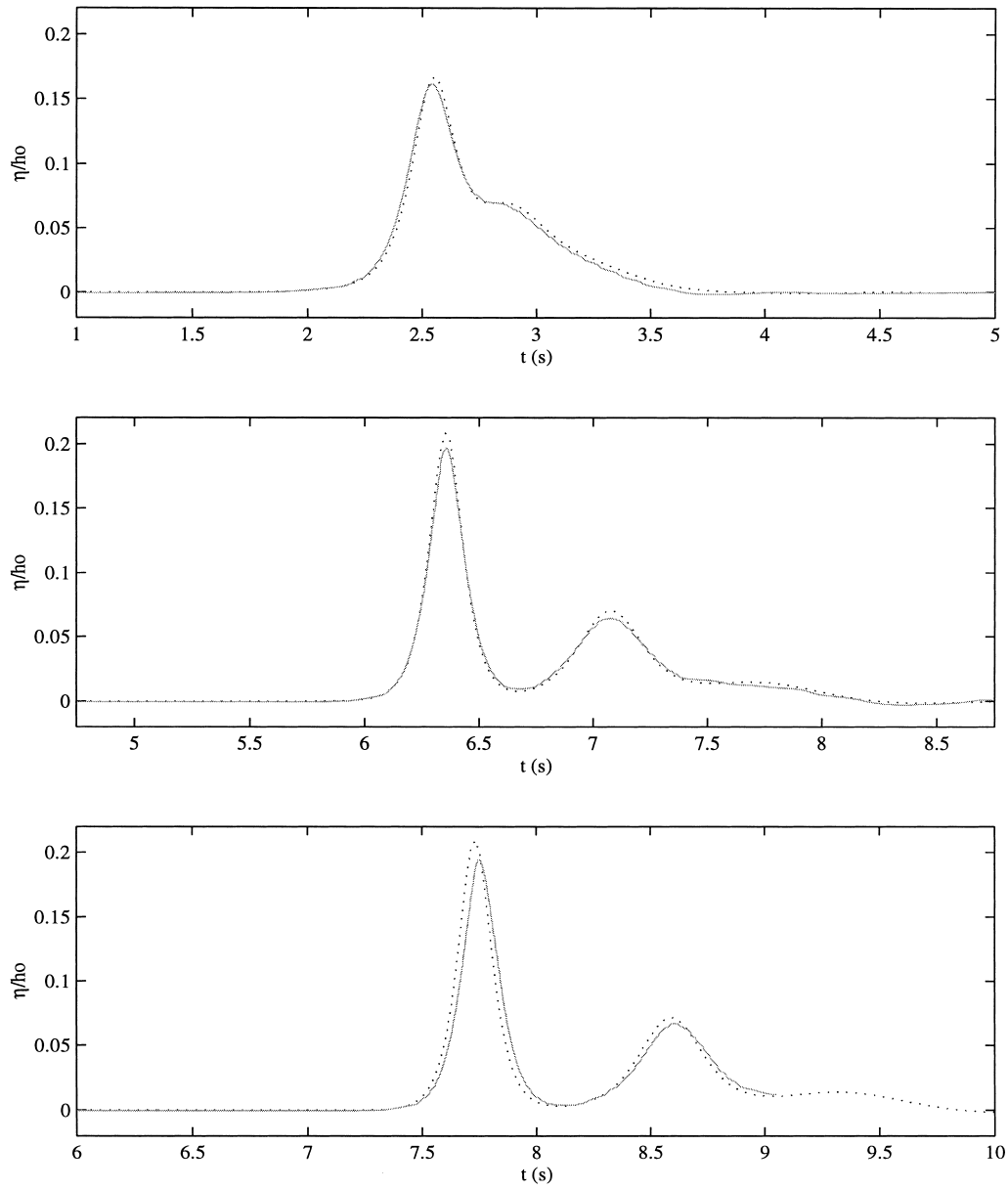

Figure 7. Comparison of time history of free surface at $x/h_0 = 27$, 57 and 70: - - - present numerical result; — Lin and Liu [25].

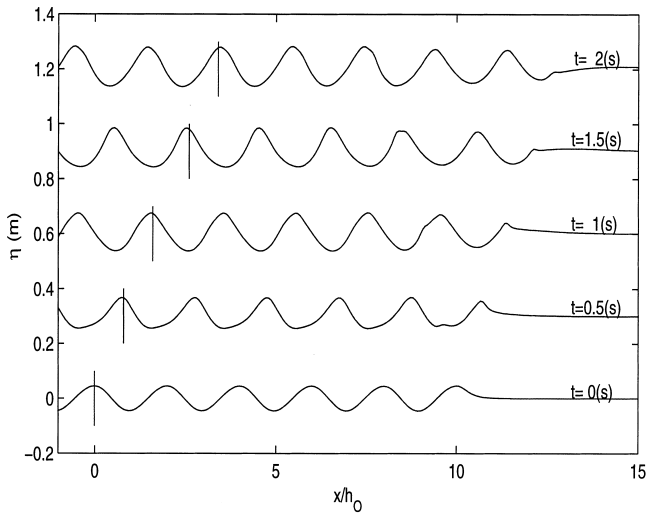

Figure 8. Numerical solutions of the extended Boussinesq equations model for the propagation of a deep water wave ($kh = 3.14$).

To test the suitability of the incident wave boundary for periodic waves in intermediate water depth, the sinusoidal wave of $kh = 1.25$, $ka = 0.01$ is generated (Figure 12). The numerical model predicts the general features of incident waves reasonably well. However, small element-size oscillations are generated near the incident wave boundary during the initial stage. Once they are generated, these high frequency waves seem to persist throughout the whole computation since the present model does not have any dissipation mechanism.

4.7. Periodic wave propagation over a bar

As shown in Figure 13, laboratory experiments have been carried out to examine the transformation of a periodic wave train over a submerged bar [26]. The experimental data have been used by several researchers to check the accuracy of their numerical models. Because of the wave decomposition taking place in the deepening region behind the bar, the wave form changes rapidly. This phenomenon can be simulated accurately only by a sufficiently non-linear model with accurate dispersion relations.

The sinusoidal wave with wave period $T = 2.857$ s, wavelength $\lambda = 7.71$ m, and wave amplitude $a = 0.04$ m is generated at the left-hand boundary and the computational domain is large enough so that the wave is not affected by the right-hand boundary. $\Delta x = 0.1$ m, $\Delta t = 0.02$ s are used so that $\lambda/\Delta x = 77$ and $T/\Delta t = 140$. Figure 14 shows the comparison of time histories of free surface profile between experimental data and numerical results at $x = 20.04$, 24.04, 26.04, 33.64, 37.04, and 41.04 m respectively.

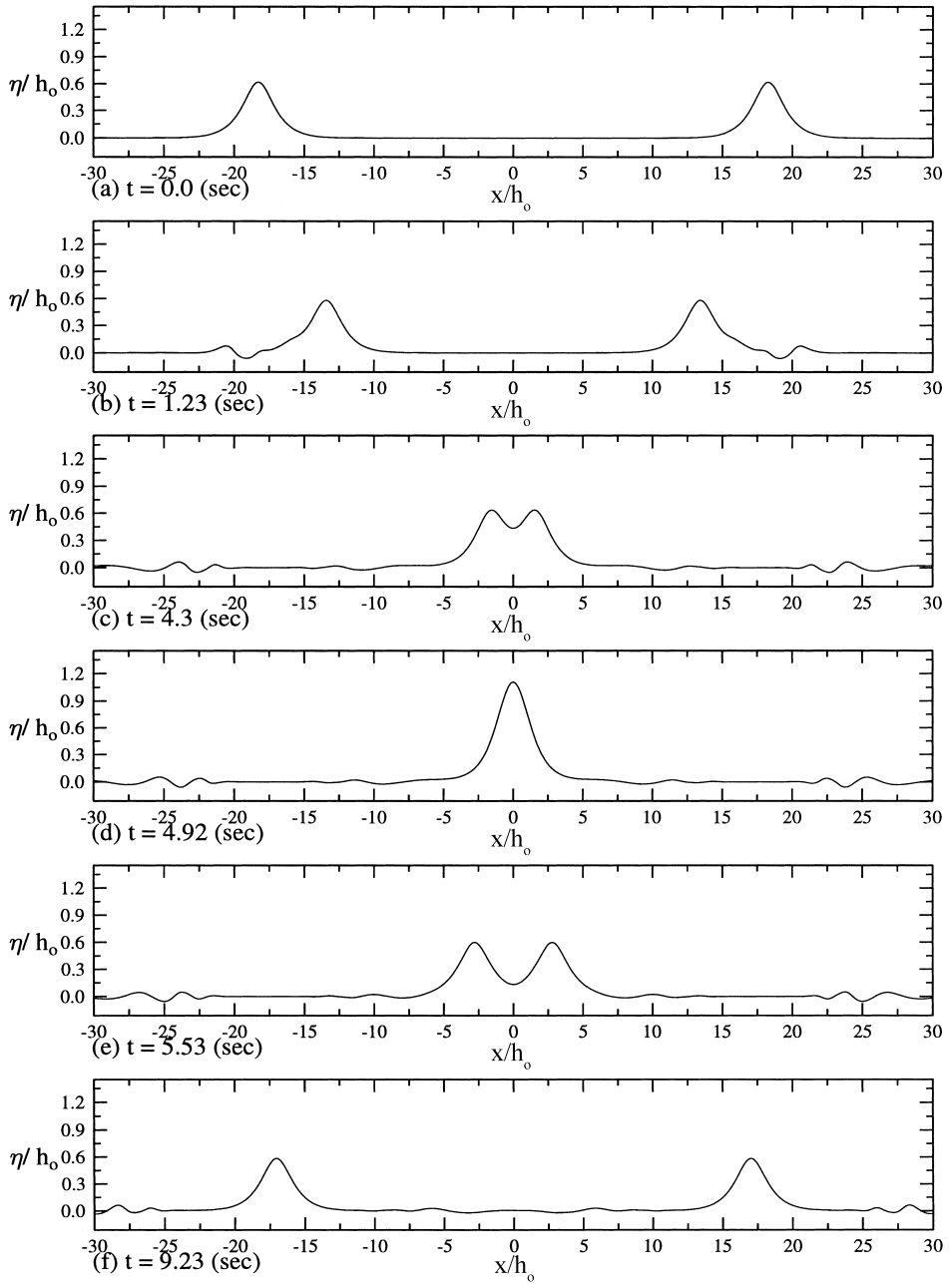

Figure 9. Interactions of solitary waves propagating in the opposite direction.

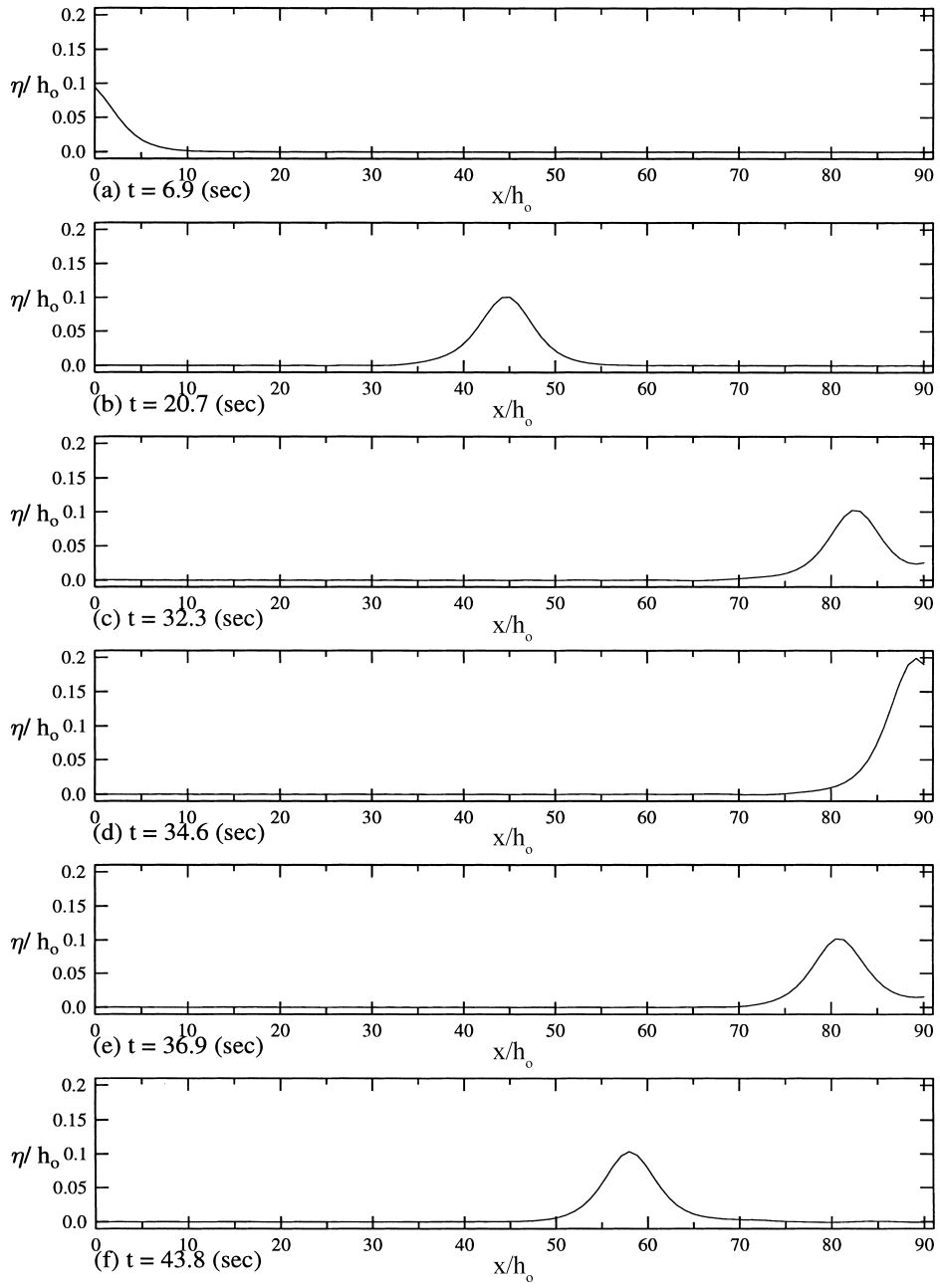

Figure 10. Numerical simulation of solitary wave propagation with incident and reflective boundary conditions ($\epsilon = 0.1$).

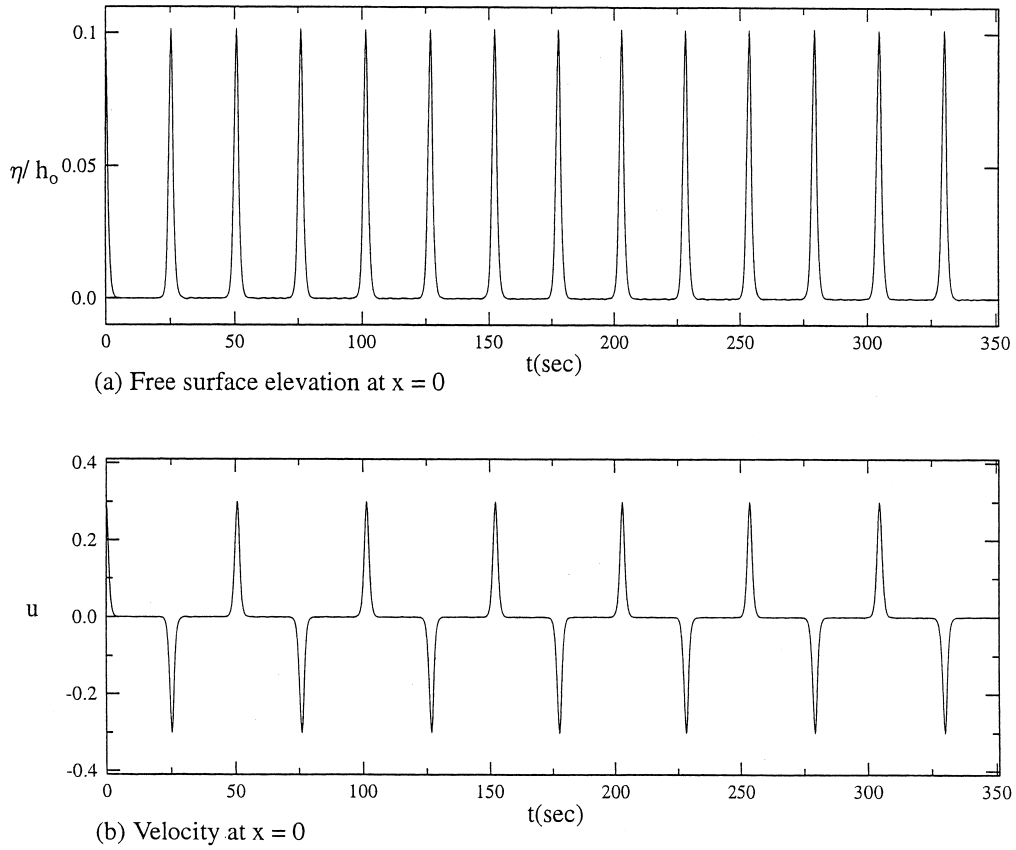

Figure 11. Time history of free surface, and velocity at $x = 0$. For the solitary wave with two reflective boundary condition ($\epsilon = 0.1$).

Up to $x = 26.04$ m, the comparisons between numerical solutions and measurements show good agreement in terms of maximum wave height and phase. The numerical model correctly resolves the higher-harmonics generation due to the nonlinear interaction at the upward slope. However, after $x = 26.04$ m, the higher-harmonic components, which become very quickly free at the downward slope, are not correctly resolved by the numerical model. As we can see in the spectral analysis (Figure 15), these free components mainly contribute to the energy distribution at frequency higher than 1 Hz. For the 1 Hz wave component, $kh = 3.46$, which is greater than the deep water limit, $kh = 3.14$. In other words, the high frequency wave components are beyond the limit of the accuracy of our governing equations, where the frequency dispersion is weak.

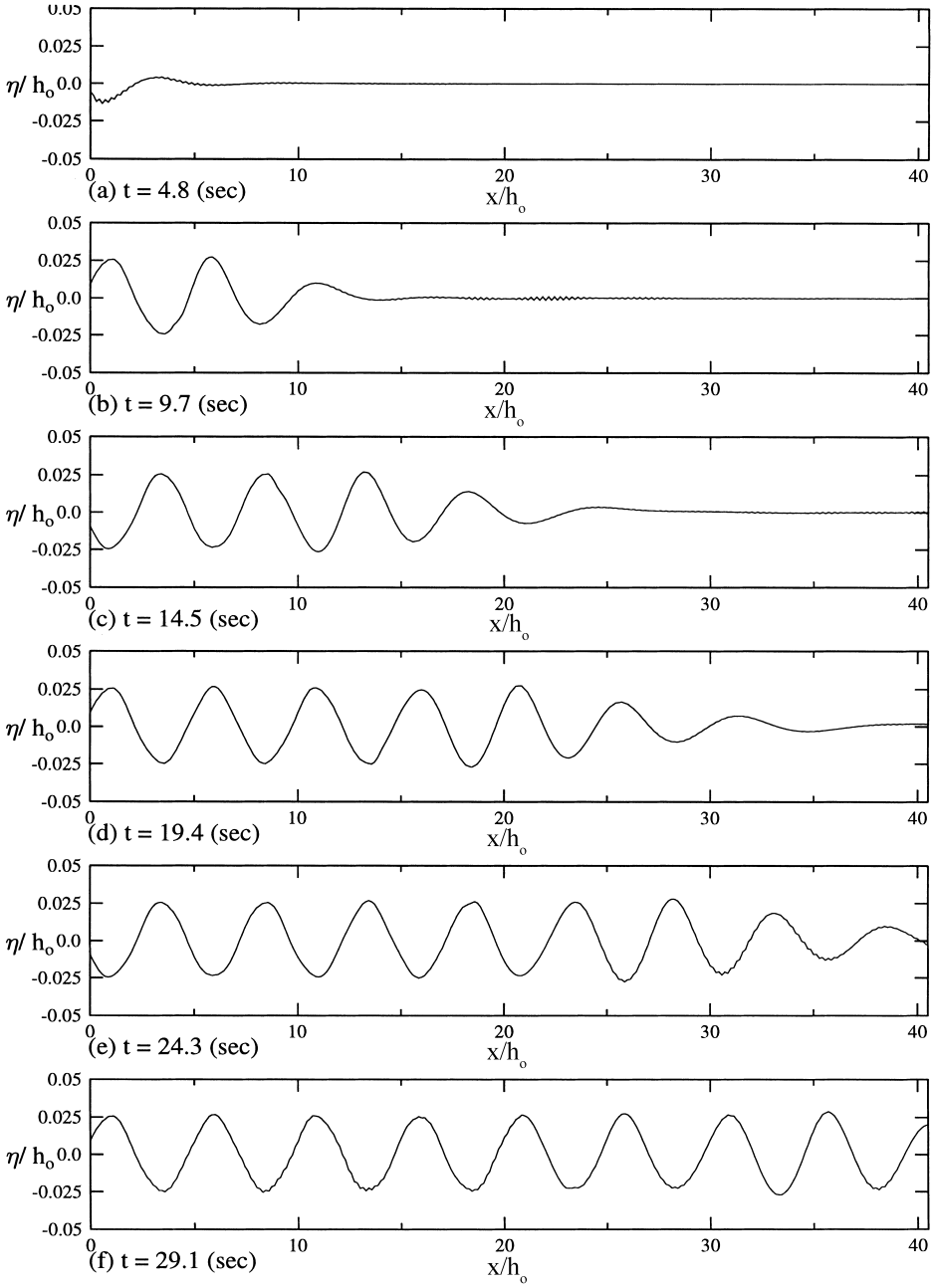

Figure 12. Sinusoidal intermediate water wave propagation through incident wave boundary condition ($kh = 1.25,\ ka = 0.01$).

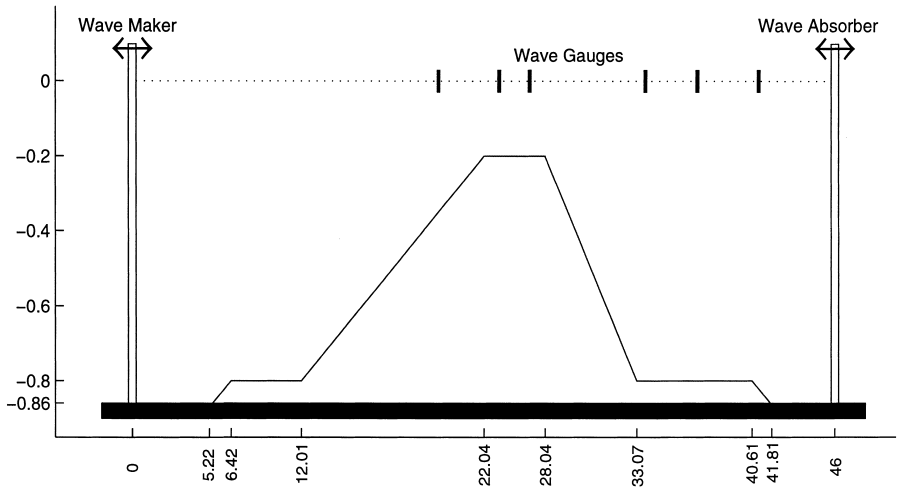

Figure 13. Layout of the submerged bar experiment (from Dingemans [26]).

5. CONCLUDING REMARKS

We have developed a Petrov–Galerkin finite element model for the one-dimensional fully non-linear and weakly dispersive wave equations. The shape functions are piecewise linear, while the weighting functions are piecewise cubic with C^2 continuity. The fourth-order Adams–Bashforth–Moulton predictor–corrector scheme is used for the time integration. Through the truncation error analysis and Von Neumann stability analysis, we have shown that the proposed scheme is fourth-order accurate in space and unconditionally stable with Courant number less than 0.5.

The numerical results for small amplitude solitary wave propagating over a distance of 1000 water depths showed that the present model is stable and conservative. The comparisons have also been made with numerical solutions, obtained from other numerical schemes, for the large amplitude solitary wave propagation, the shoaling of solitary wave, and the fission of solitary wave. The good agreement confirms the accuracy of the present model in treating the non-linear terms. Also the simulation of deep-water wave propagation illustrates that the improved dispersion relationship is well resolved by the model. The model is still limited to weakly dispersive systems, so that the higher harmonic free waves that appear at the back of the submerged bar cannot be captured accurately by the present model.

It is straightforward to extend the present Petrov–Galerkin FEM to a two-dimensional domain with non-uniform structured quadrilateral grids [27]. However, applying this method to unstructured grids would be quite challenging. Recently, attempts have been made to develop piecewise C^1-type functions over unstructured meshes [28,29]. In our opinion, it is possible to extend the present approach to a two-dimensional domain with unstructured grids, although the computational costs for mapping the C^1-type weighting function over an unstructured mesh need to be carefully considered.

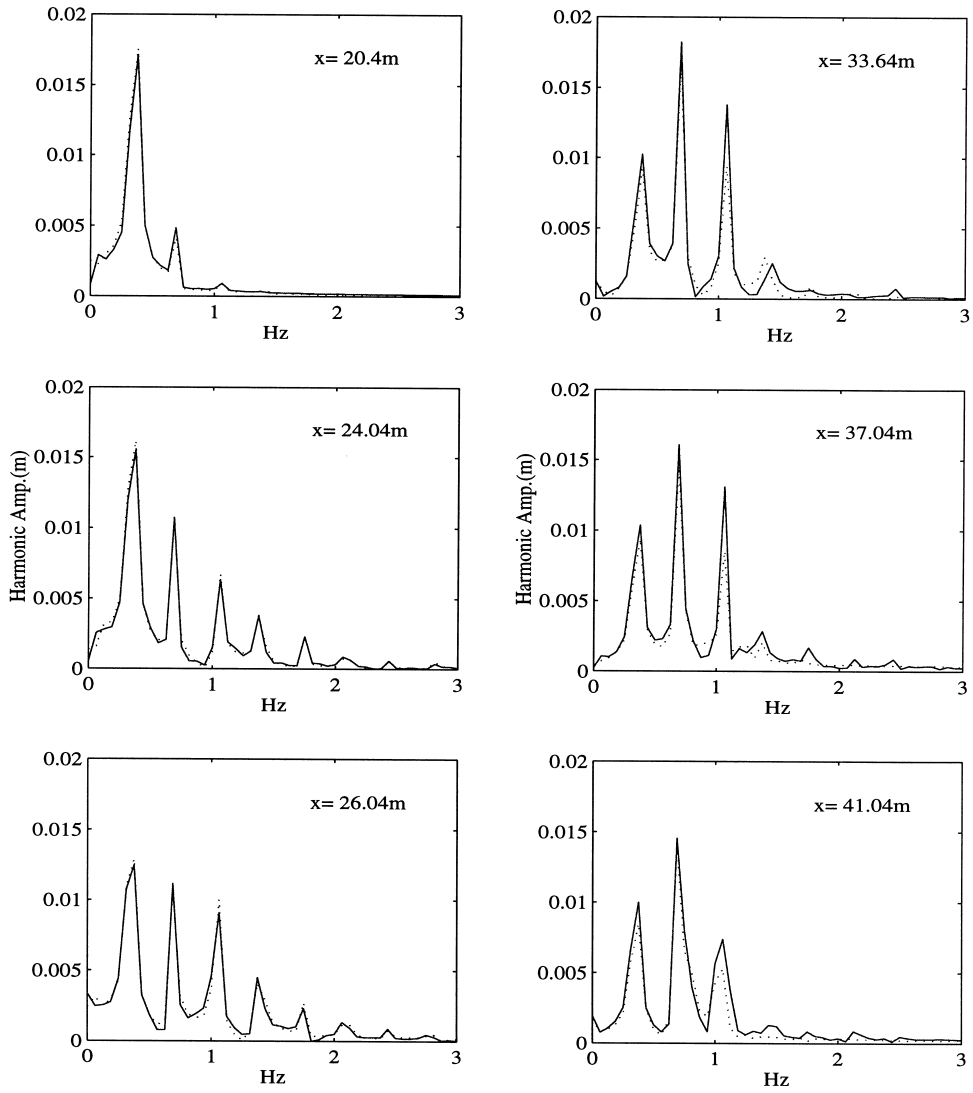

Figure 15. Comparisons of amplitude spectrum of measured data and present FEM solutions: — present numerical result; · · · experiment.

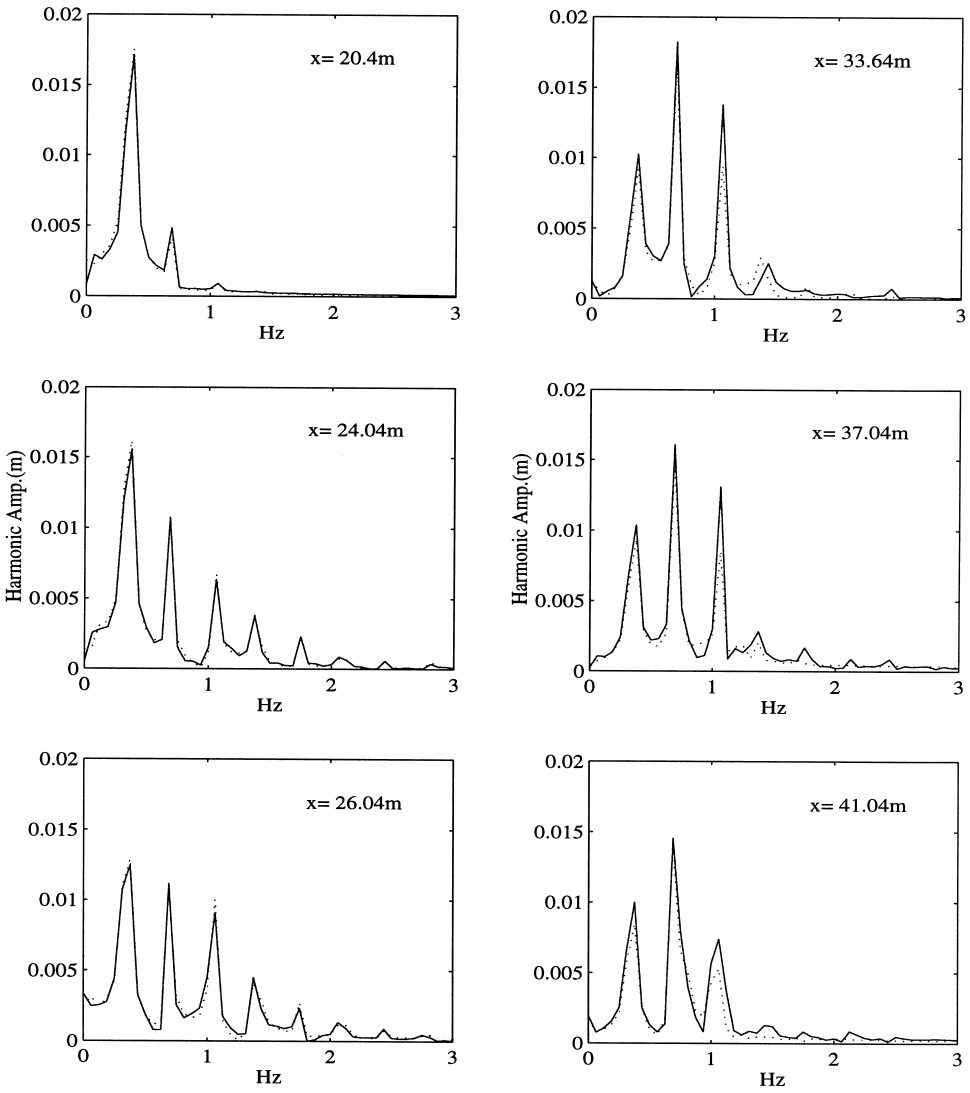

Figure 15. Comparisons of amplitude spectrum of measured data and present FEM solutions: — present numerical result; · · · experiment.

ACKNOWLEDGMENTS

This research has been supported, in part, by a research grant from National Science Foundation to Cornell University (BES-9714182).

APPENDIX A. MASS MATRIX, FORCING VECTOR AND BOUNDARY VECTOR

Let us introduce the following notations:

$$\Phi_j^p := \frac{\mathrm{d}^p \phi_j}{\mathrm{d}x^p}$$

$$\Psi_j^p := \frac{\mathrm{d}^p \psi_j}{\mathrm{d}x^p}$$

in which ϕ_j is the weighting function and ψ_j the shape function. The superscript means the order of derivative. When p is zero

$$\Phi_j^0 := \frac{\mathrm{d}^0 \phi_j}{\mathrm{d}x^0} := \phi_j$$

is implied. Therefore, the superscript 0 will be omitted.

The mass matrices in (3.7) and (3.8) can be defined as

$$[M^u]_{ij}^n = [M_1^u]_{ij} + \mu^2 [M_2^u]_{ij} + \varepsilon\mu^2 [\tilde{M}_1^u]_{ij}^n + \varepsilon^2\mu^2 [\tilde{M}_2^u]_{ij}^n \tag{A.1}$$

where

$$[M_1^u]_{ij} = [M^\eta]_{ij} = \langle \Phi_i \Psi_j \rangle \tag{A.2}$$

$$\begin{aligned}[M_2^u]_{ij} = & -C_4 \sum_k \langle \Phi_i \Psi_k^1 \Psi_j^1 \rangle (\{h\}_k)^2 - \beta \sum_k \sum_l \langle \Phi_i \Psi_k^1 \Psi_l^1 \Psi_j \rangle \{h\}_k \{h\}_l \\ & - C_5 \sum_k \langle \Phi_i^1 \Psi_k \Psi_j^1 \rangle (\{h\}_k)^2 - \frac{\beta}{2} \sum_k \langle \Phi_i^1 \Psi_k^1 \Psi_j \rangle (\{h\}_k)^2 \end{aligned} \tag{A.3}$$

$$[\tilde{M}_1^u]_{ij}^n = -\sum_k \sum_l \langle \Phi_i^1 \Psi_k \Psi_l^1 \Psi_j \rangle \{h\}_k \{\eta\}_l^n - \sum_k \langle \Psi_i^2 \Psi_k \Psi_j \rangle \{h\}_k \{\eta\}_k^n \tag{A.4}$$

$$[\tilde{M}_2^u]_{ij}^n = -\frac{1}{2} \sum_k \langle \Phi_i^1 \Psi_k^1 \Psi_j \rangle (\{\eta\}_k^n)^2 - \frac{1}{2} \sum_k \langle \Phi_i^2 \Psi_k \Psi_j \rangle (\{\eta\}_k^n)^2 \tag{A.5}$$

in which $\langle \cdot \rangle$ denotes $\int_{x_j}^{x_{j+1}} \cdot \, \mathrm{d}x$ and Σ_k denotes $\Sigma_{k=0}^J$.

The forcing vectors in (3.7) and (3.8) have the following expressions:

$$\{f^n\}_i^n = \{f_1^n\}_i^n + \varepsilon\{f_2^n\}_i^n + \mu^2\{f_3^n\}_i^n + \varepsilon\mu^2\{f_4^n\}_i^n + \varepsilon^2\mu^2\{f_5^n\}_i^n + \varepsilon^3\mu^2\{f_6^n\}_i^n \tag{A.6}$$

$$\{f^u\}_i^n = \{f_1^u\}_i^n + \varepsilon\{f_2^u\}_i^n + \varepsilon\mu^2\{f_3^u\}_i^n + \varepsilon^2\mu^2\{f_4^u\}_i^n + \varepsilon^3\mu^2\{f_5^u\}_i^n \tag{A.7}$$

in which

$$\{f_1^u\}_i^n = \sum_k \langle \Phi_i^1 \Psi_k \rangle \{\eta\}_k^n \tag{A.8}$$

$$\{f_2^u\}_i^n = \frac{1}{2} \sum_k \langle \Phi_i^1 \Psi_k \rangle (\{u_\alpha\}_k^n)^2 \tag{A.9}$$

$$\begin{aligned}\{f_3^u\}_i^n = & -\sum_k \sum_l \langle \Phi_i^1 \Psi_k^1 \Psi_l^1 \rangle \left[C_2 (\{h\}_k)^2 \{u_\alpha\}_k^n \{u\}_l^n + \left(\beta - \frac{1}{2}\right) \{h\}_k \{u_\alpha\}_k^n \{h\}_l \{u_\alpha\}_l^n \right] \\ & - \sum_k \sum_l \left[\frac{C^2}{2} \langle \Phi_i^2 \Psi_k \Psi_l^1 \rangle (\{h\}_k)^2 (\{u_\alpha\}_l^n)^2 + \frac{\beta}{2} \langle \Phi_i^2 \Psi_k^1 \rangle (\{h\}_k \{u_\alpha\}_k^n)^2 \right]\end{aligned} \tag{A.10}$$

$$\begin{aligned}\{f_4^u\}_i^n = & \sum_k \sum_l \left[\langle \Phi_i^1 \Psi_k^1 \Psi_l^1 \rangle \{\eta\}_k^n \{u_\alpha\}_k^n \{h\}_l \{u_\alpha\}_l^n + \sum_m \langle \Phi_i^1 \Psi_k \Psi_l^1 \Psi_m^1 \rangle \{\eta\}_k^n \{u_\alpha\}_l^n \{h\}_m \{u_\alpha\}_m^n \right. \\ & \left. + \langle \Phi_i^2 \Psi_k \Psi_l^1 \rangle \{\eta\}_k^n \{u_\alpha\}_k^n \{h\}_l \{u_\alpha\}_l^n \right]\end{aligned} \tag{A.11}$$

$$\begin{aligned}\{f_5^u\}_i^n = & \sum_k \sum_l \left[\frac{1}{2} \langle \Phi_i^1 \Psi_k^1 \Psi_l^1 \rangle (\{\eta\}_k^n)^2 \{u_\alpha\}_k^n \{u_\alpha\}_l^n + \sum_m \frac{1}{2} \langle \Phi_i^1 \Psi_k \Psi_l^1 \Psi_m^1 \rangle (\{\eta\}_k^n)^2 \{u_\alpha\}_l^n \{u_\alpha\}_m^n \right. \\ & \left. + \frac{1}{4} \langle \Phi_i^2 \Psi_k \Psi_l^1 \rangle (\{\eta\}_k^n)^2 (\{u_\alpha\}_l^n)^2 \right]\end{aligned} \tag{A.12}$$

$$\{f_1^\eta\}_i^n = \sum_k \langle \Phi_i^1 \Psi_k \rangle \{h\}_k \{u_\alpha\}_k^n \tag{A.13}$$

$$\{f_2^\eta\}_i^n = \sum_k \langle \Phi_i^1 \Psi_k \rangle \{\eta\}_k^n \{u_\alpha\}_k^n \tag{A.14}$$

$$\{f_3^\eta\}_i^n = -\sum_k \sum_l \langle \Phi_i^1 \Psi_k^1 \Psi_l^1 + \Phi_i^2 \Psi_k \Psi_l^1 \rangle [C_1 (\{h\}_k)^3 \{u_\alpha\}_l^n + C_3 (\{h\}_k)^2 \{h\}_l \{u_\alpha\}_l^n] \tag{A.15}$$

$$\{f_4^\eta\}_i^n = -\sum_k \sum_l \langle \Phi_i^1 \Psi_k^1 \Psi_l^1 + \Phi_i^2 \Psi_k \Psi_l^1 \rangle [C_2 (\{h\}_k)^2 \{\eta\}_k^n \{u_\alpha\}_l^n + \beta \{h\}_k \{\eta\}_k^n \{h\}_l \{u_\alpha\}_l^n] \tag{A.16}$$

$$\{f_5^\eta\}_i^n = \frac{1}{2} \sum_k \sum_l \langle \Phi_i^1 \Psi_k^1 \Psi_l^1 + \Phi_i^2 \Psi_k \Psi_l^1 \rangle (\{\eta\}_k^n)^2 \{h\}_l \{u_\alpha\}_l^n \tag{A.17}$$

$$\{f_6^\eta\}_i^n = \frac{1}{6} \sum_k \sum_l \langle \Phi_i^1 \Psi_k^1 \Psi_l^1 + \Phi_i^2 \Psi_k \Psi_l^1 \rangle (\{\eta\}_k^n)^3 \{u_\alpha\}_l^n \tag{A.18}$$

We have used the product approximation technique for the non-linear terms as shown in, for example, (A.9). The weak forms (3.3) and (3.4) have been written in such a way that they contain the divergence form as much as possible so as to apply the product approximation technique for the higher non-linear terms.

Finally, the boundary vectors in (3.7) and (3.8) can be expressed as

$$\{q^{\eta}\}_i^n = \{q_1^{\eta}\}_i^n + \varepsilon\{q_2^{\eta}\}_i^n + \mu^2\{q_3^{\eta}\}_i^n + \varepsilon\mu^2\{q_4^{\eta}\}_i^n + \varepsilon^2\mu^2\{q_5^{\eta}\}_i^n + \varepsilon^3\mu^2\{q_6^{\eta}\}_i^n \tag{A.19}$$

$$\{q^{u}\}_i^n = \{q_1^{u}\}_i^n + \varepsilon\{q_2^{u}\}_i^n + \mu^2\{q_3^{u}\}_i^n + \varepsilon\mu^2\{q_4^{u}\}_i^n + \varepsilon^2\mu^2\{q_5^{u}\}_i^n + \varepsilon^3\mu^2\{q_6^{u}\}_i^n \tag{A.20}$$

in which

$$\{q_1^{\eta}\}_i^n = -\sum_k [\Phi_i\Psi_k\{h\}_k\{u_\alpha\}_k^n]\Big|_{x_j}^{x_{j+1}} \tag{A.21}$$

$$\{q_2^{\eta}\}_i^n = -\sum_k [\Phi_i\Psi_k\{\eta\}_k^n\{u_\alpha\}_k^n]\Big|_{x_j}^{x_{j+1}} \tag{A.22}$$

$$\{q_3^{\eta}\}_i^n = -\sum_k\sum_l [(\Phi_i\Psi_k\Psi_l^2 - \Phi_i^1\Psi_k\Psi_l^1)(C_1(\{h\}_k)^3\{u_\alpha\}_l^n + C_3(\{h\}_k)^2\{h\}_l\{u_\alpha\}_l^n)]\Big|_{x_j}^{x_{j+1}} \tag{A.23}$$

$$\{q_4^{\eta}\}_i^n = -\sum_k\sum_l [(\Phi_i\Psi_k\Psi_l^2 - \Phi_i^1\Psi_k\Psi_l^1)(C_2(\{h\}_k)^2\{\eta\}_k^n\{u_\alpha\}_l^n + \beta\{h\}_k\{\eta\}_k^n\{h\}_l\{u_\alpha\}_l^n)]\Big|_{x_k}^{x_{j+1}} \tag{A.24}$$

$$\{q_5^{\eta}\}_i^n = \sum_k\sum_l \left[\frac{1}{2}\Phi_i\Psi_k\Psi_l^2(\{\eta\}_k^n)^2\{h\}_l\{u\}_l^n - \frac{1}{6}\Phi_i^1\Psi_k\Psi_l^1(\{\eta\}_k^n)^3\{u_\alpha\}_l^n\right]\Bigg|_{x_j}^{x_{j+1}} \tag{A.25}$$

$$\{q_1^{u}\}_i^n = -\sum_k [\Phi_i\Psi_k\{\eta\}_k^n]\Big|_{x_j}^{x_{j+1}} \tag{A.26}$$

$$\{q_2^{u}\}_i^n = -\frac{1}{2}\sum_k [\Phi_i\Psi_k(\{u_\alpha\}_k^n)^2]\Big|_{x_j}^{x_{j+1}} \tag{A.27}$$

$$\{q_3^{u}\}_i^n = -\sum_k\sum_l [\Phi_i\Psi_k\Psi_l^1(C_2(\{h\}_k)^2\{\dot{u}_\alpha\}_l^n + \beta\{h\}_k\{h\}_l\{\dot{u}_\alpha\}_l^n)]\Big|_{x_j}^{x_{j+1}} \tag{A.28}$$

$$\{q_4^{u}\}_i^n = -\sum_k\sum_l \left[\beta\Phi_i\Psi_k\Psi_l^2\{h\}_k\{u_\alpha\}_k^n\{h\}_l\{u_\alpha\}_l^n + C_2\Phi_i\Psi_k\Psi_l^2(\{h\}_k)^2\{u_\alpha\}_k^n\{u_\alpha\}_l^n + \frac{1}{2}\Phi_i\Psi_k^1\Psi_l^1\{h\}_k\{u_\alpha\}_k^n\{h\}_l\{u_\alpha\}_l^n - \Phi_i\Psi_k\Psi_l^1\{\eta\}_k^n\{h\}_l\{\dot{u}_\alpha\}_l^n\right]\Bigg|_{x_j}^{x_{j+1}}$$

$$+\sum_k \sum_l \left[\Phi_i^1 \Psi_k \Psi_l^1 \left(\frac{C_2}{2} (\{h\}_k)^2 (\{u_\alpha\}_l^n)^2 + \beta \{h\}_k \{u_\alpha\}_k^n \{h\}_l \{u_\alpha\}_l^n \right) - \Phi_i^1 \Psi_k \{h\}_k \{\eta\}_k^n \{\dot{u}_\alpha\}_k^n \right]_{x_j}^{x_{j+1}} \tag{A.29}$$

$$\{q_5^u\}_i^n = \sum_k \sum_l \left[\Phi_i \Psi_k \Psi_l^2 \{\eta\}_k^n \{u_\alpha\}_k^n \{h\}_l \{u_\alpha\}_l^n - \sum_m \Phi_i \Psi_k \Psi_l^1 \psi_m^1 \{\eta\}_k^n \{u_\alpha\}_l^n \{h\}_m \{u_\alpha\}_m^n + \frac{1}{2} \Phi_i \Psi_k \Psi_l^1 (\{\eta\}_k^n)^2 \{\dot{u}_\alpha\}_l^n \right]_{x_j}^{x_{j+1}}$$
$$- \sum_k \sum_l \left[\Phi_i^1 \Psi_k \Psi_l^1 \{\eta\}_k^n \{u_\alpha\}_k^n \{h\}_l \{u_\alpha\}_l^n + \frac{1}{2} \Phi_i^1 \Psi_k (\{\eta\}_k^n)^2 \{\dot{u}_\alpha\}_k^n \right]_{x_j}^{x_{j+1}} \tag{A.30}$$

$$\{q_6^u\}_i^n = \sum_k \sum_l \left[\Phi_i \Psi_k \Psi_l^2 \frac{1}{2} (\{\eta\}_k^n)^2 \{u_\alpha\}_k^n \{u_\alpha\}_l^n - \frac{1}{2} \sum_m \Phi_i \Psi_k \Psi_l^1 \Psi_m^1 (\{\eta\}_k^n)^2 \{u_\alpha\}_l^n \{u_\alpha\}_m^n \right]_{x_j}^{x_{j+1}}$$
$$- \sum_k \sum_l \left[\Phi_i^1 \Psi_k \Psi_l^1 \frac{1}{4} (\{\eta\}_k^n)^2 (\{u_\alpha\}_l^n)^2 \right]_{x_j}^{x_{j+1}} \tag{A.31}$$

REFERENCES

1. Liu PL-F. Model equations for wave propagations from deep to shallow water. In *Advances in Coastal and Ocean Engineering*, vol. 1, Liu PL-F (ed.). World Scientific Publishing: Singapore, 1994; 125–157.
2. Wei G, Kirby JT, Grilli ST, Subramanya R. A fully nonlinear Boussinesq model for surface waves. Part 1. Highly nonlinear unsteady waves. *Journal of Fluid Mechanics* 1995; **294**: 71–92.
3. Madsen PA, Schäffer HA. Higher-order Boussinesq-type equations for surface gravity waves: Derivation and analysis. *Philosophical Transcripts of the Royal Society of London A* 1998; **356**: 2123–3184.
4. Gobbi MF, Kirby JT. Wave evolution over submerged sills: tests of a high-order Boussinesq model. *Coastal Engineering* 1999; **37**: 57–96.
5. Abbott MB, McCowan AD, Warren IR. Accuracy of short wave numerical models. *Journal of Hydraulic Engineering* 1984; **110**(10): 1287–1301.
6. Wei G, Kirby JT. Time-dependent numerical code for extended Boussinesq equations. *ASCE Journal of Waterway*, *Port*, *Coastal and Ocean Engineering* 1995; **121**: 251–261.
7. Beji S, Nadaoka K. A formal derivation and numerical modeling of the improved Boussinesq equations for varying depth. *Ocean Engineering* 1996; **23**(8): 691–704.
8. Katopodes ND, Wu C. Computation of finite-amplitude dispersive waves. *ASCE Journal of Waterway*, *Port*, *Coastal*, *and Ocean Engineering* 1987; **113**(4): 327–346.
9. Antunes do Carmo JS, Seabra Santos FJ, Barthelemy E. Surface waves propagation in shallow water: A finite element model. *International Journal for Numerical Methods in Fluids* 1993; **16**: 447–459.
10. Kawahara M, Cheng JY. Finite element method for Boussinesq wave analysis. *International Journal of Computational Fluid Dynamics* 1994; **2**: 1–17.
11. Langtangen HP, Pedersen G. Finite elements for the Boussinesq wave equations. In *Waves and Nonlinear Processes in Hydrodynamics*, Grue J, Gjeviki G, Weber JE (eds). Kluwer Academic: Dordrecht, 1996; 1–10.
12. Ambrosi D, Quartapelle L. A Taylor–Galerkin method for simulating nonlinear-dispersive water waves. *Journal of Computational Physics* 1998; **146**: 546–569.
13. Antunes do Carmo JS, Seabra Santos FJ. On breaking waves and wave-current interaction in shallow water: a 2DH finite element model. *International Journal for Numerical Methods in Fluids* 1996; **22**: 429–444.
14. Li YS, Liu S-X, Yu Y-X, Lai G-Z. Numerical modeling of Boussinesq equations by finite element method. *Coastal Engineering* 1999; **37**: 97–122.
15. Walkley M, Berzins M. A Finite element method for the one-dimensional extended Boussinesq equations. *International Journal for Numerical Methods in Fluids* 1999; **29**: 143–157.

16. Sanz-Serna JM, Christie I. Petrov–Galerkin methods for nonlinear dispersive waves. *Journal of Computational Physics* 1981; **39**: 94–102.
17. Mitchell AR, Weit R. *The Finite Element Method in Partial Differential Equations*. Wiley: New York, 1977.
18. Tourigny Y, Morris JL. An investigation into the effect of product approximation in the numerical solution of the cubic nonlinear Schrödinger equation. *Journal of Computational Physics* 1988; **76**: 103–130.
19. Chen Y, Liu PL-F. Modified Boussinesq equations and associated parabolic models for wave propagation. *Journal of Fluid Mechanics* 1995; **288**: 351–381.
20. Nwogu O. An alternative form of the Boussinesq equations for nearshore wave propagation. *Journal of Waterway, Port, Coastal, and Ocean Engineering* 1993; **119**: 618–638.
21. Gardner LRT, Gardner GA. Solitary waves of the regularised long-wave equation. *Journal of Computational Physics* 1990; **91**: 441–459.
22. Goring DG. Tsunamis—the propagation of long waves onto a shelf. PhD thesis, California Institute of Technology, 1979.
23. Grilli ST, Skourup J, Svendsen IA. An efficient boundary element method for nonlinear water waves. *Engineering Analysis with Boundary Elements* 1989; **6**: 97–107.
24. Grilli ST, Subramanya R, Svendsen IA, Veeramony J. Shoaling of solitary waves on place beaches. *ASCE Journal of Waterway, Port, Coastal, and Ocean Engineering* 1994; **120**: 609–628.
25. Lin P, Liu PL-F. A numerical study of breaking waves in the surf zone. *Journal of Fluid Mechanics* 1998; **359**: 239–264.
26. Dingemans MW. Comparison of computations with Boussinesq-like models and laboratory measurements. Technical Report H1684.12, MAST G8M Coastal Morphodynamics Research Programme, 1994.
27. Gardner LRT, Gardner GA. A two dimensional bi-cubic B-spline finite element: used in a study of MHD-duct flow. *Computer Methods in Applied Mechanics and Engineering* 1995; **124**: 365–375.
28. Alfeld P, Piper B, Schumaker LL. An explicit basis for C1 quartic bivariate splines. *SIAM Journal of Numerical Analysis* 1987; **24**(4): 891–911.
29. Sabin MA. Spline finite elements. PhD Thesis, University of Cambridge, 1997.

